Examining the Heterojunction between Active Layers in Poly(3-hexylthiophene-2,5-diyl) / [6,6]-Penyl-C61-butyric-acid-methyl-ester Photovoltaic Devices

by

Phoebe Tengdin

Submitted to the Department of Physics
in partial fulfillment of the requirements for the degree of

Bachelors of Arts

at

Mount Holyoke College

May 2013

Author .....
Department of Physics
May 1, 2013

Certified by .....
Alexi C. Arango
Assistant Professor of Physics
Thesis Supervisor

Accepted by .....
Janice Hudgings
Chair, Department of Physics

Examining the Heterojunction between Active Layers in Poly(3-hexylthiophene-2,5-diyl) / [6,6]-Penyl-C61-butyric-acid-methyl-ester Photovoltaic Devices

by

Phoebe Tengdin

Submitted to the Department of Physics
on May 1, 2013, in partial fulfillment of the
requirements for the degree of
Bachelors of Arts

Abstract

Organic photovoltaic devices consist of materials that are cheap, flexible, and easy to process, yet typically low in efficiency. A primary method of improving the efficiencies of these devices is to mix of the active layers of the device into a single solution, forming a bulk heterojunction when deposited. This method is easier to accomplish than depositing each layer separately, and increases the surface area of the interface between the materials while decreasing the distance required for an exciton to travel before disassociating across the heterojunction, contributing to an increase in device efficiency. However, some drawbacks of this design include limited control over nanoscale features in the device, and the increase in interfacial recombination and leakage currents leading to lower open circuit voltage. We present an alternative to the bulk heterojunction device structure by demonstrating the success of a recently developed method of depositing solution processed molecular materials. Our method employs stamping of the electron acceptor layer, [6,6]-penyl-C61-butyric-acid-methyl-ester (PCBM), on top of a spin-coated hole acceptor layer, poly(3-hexylthiophene-2,5-diyl) (P3HT). This fabrication process results in a planar heterojunction geometry. Solar cells fabricated in this way have a smaller donor-acceptor interfacial area for exciton dissociation, but better defined pathways for charge collection, potentially resulting in decreased short circuit current but improved shunt resistance. Additionally, these cells are better suited for fundamental studies of organic-organic interfaces, because of the inherent control over the thickness and concentration of each organic layer.

We analyze the morphology of the active layers in our device through the use of an atomic force microscope and find the film's RMS roughness to be 15.1nm. We conclude that the roughness of the P3HT surface should contribute to a large contact area between the P3HT and PCBM films, and possibly a mixed layer of material in the interface between the two layers. We present the current-voltage characteristics of our bi-layer devices and compare their performance to bulk heterojunction devices fabricated within the same laboratory conditions. Our highest efficiency P3HT:PCBM bulk heterojunction devices have J_{SC}=5.5mA with V_{OC}=0.35V and FF=0.07, while our most efficient P3HT/PCBM planar heterojunction devices have J_{SC} = 3.45x10^{-3}mA, V_{OC}=0.1V and FF=0.021. These results demonstrate great promise for our laboratory, which has only just begun to fabricate bulk heterojunction devices, and is now generating new devices with cutting-edge fabrication techniques. We compare our results to an analytical model for bi-layer devices based on the diffusion equation for exciton generation and the drift-diffusion equations for charge transport within the device. This model shows good agreement with experiments. Additionally, we ran monte carlo simulations for charge generation and transport in the organic materials and analyzed the results of these simulations. Our analysis found physical inconsistencies in these simulations, and further work will be necessary to understand the errors in this model before it can be compared to our experimental results.

Thesis Supervisor: Alexi C. Arango
Title: Assistant Professor of Physics

Acknowledgments

My first acknowledgement goes to Alexi Arango, who provided me with the encouragement, support, and detailed knowledge necessary to complete this thesis. Since I first began working with Professor Arango in my sophomore year, he has been a constant source of inspiration and enthusiasm for me both in my laboratory work, and through advising me with my coursework. He constantly stands out as a brilliant role model. I have striven to model my pursuit of a career in physics after his inspiring example.

Next, I want to thank the entire Arango lab group, and particularly: Sophia, because she is an amazing friend and also helped me enormously while we both wrote our senior theses together; Emily, because she helped me so much in understanding device characterization and because she is just an awesome person to be around; Andrea, who also wrote her thesis alongside me, and helped me in so many ways, particularly by characterizing my samples with the AFM; Maggie, who helped me with fabrication and was always willing to come in and help with my experiments; Kanchi, because of all the late nights we've spent together discussing physics and life; Husna, for staying in the lab with me over spring break and always being excited about research and willing learn; Shola, because her face is ridiculous; Rudo, for all of the late nights we've spent in the lounge together; Laalitya, for her sense of humor and ability to always make me laugh; Shehzeen, for helping me with characterization and her dedication to the lab (even while studying at another university!) and Georgina and Sadia who helped building the lab last summer.

I need to thank the entire physics department community at Mount Holyoke; it has been my priviledge to spend four years in this wonderful environment. I wish to personally thank Tav Hawkings, who first taught me how to think about physics; Janice Hudgings, who gave me great encouragement in my sophomore year; Mark Peterson, who taught me how beautiful physics can

be and whose constant enthusiasm has been a great example to me; Juan Burciaga, who is an amazing example because he is always interested in helping students understand a physics problem no matter what time of the day or night it is; and Kathy Aidala who showed me how to apply all of my physics knowledge to useful things in electronics. All of these professors taught my physics classes with an unmatched enthusiasm and impressive rigor. I would also like to thank several professors from the mathematics department: Jillian McLeod, who first encouraged me in my first year that I could be successful in physics, Jessica Sidman, who gave me invaluable advice on which math classes are useful to a physics major; and Matthew Noonan, whose fascinating class and unwavering work ethic both challenged me and renewed my love for physics and math.

Separately, I want to thank Kathy Aidala and Jessica Sidman for serving on my thesis commmittee and giving me valuable feedback on this work. Your insightful questions at my defense helped me think through some interesting topics, and your attention to detail throughout this entire process has made this document possible.

Finally I want to thank all of my friends at Mount Holyoke who have supported me throughout my time here. Particularly I want to thank the Mount Holyoke cross country team, for keeping me sane, and giving me an external support network through our daily runs and weekly races. Thank you to Jennifer Adams, our coach, and to my close friends and workout buddies on the team: Felicia, Jenna, Lucy, Liz, Dana, Ellie, and Rose. You guys are the best cure for a rough day in the lab.

Last, thank you to my family: Doug, Pam, David, Priscilla, Drew, Daniel, and Dean who have all been there for me during the last four years. Your constant support has truly made my studies possible.

Contents

List of Figures

List of Tables

Chapter 1

Introduction

This chapter will introduce the reader to solar cells through a brief history of their development and a report of the current state of research today. These electronic devices have recently received intense research attention due to the current global energy crisis and movement towards renewable energy sources. The energy output of the sun is enormous; its power utilized by almost all forms of life on Earth. The sun is the greatest source of energy in our environment, hitting earth with over three times as much energy in one day than all of our natural resources combined could muster [1].

When humans can employ earth-abundant materials to harvest this energy for our own purposes, we will have the ability to satisfy our current energy demands indefinitely. This chapter will cover a brief history of the discovery of the photovoltaic effect, invention of the solar cell, and subsequent recent developments. We will describe our work, which concentrates on organic photovoltaic devices, solar cells made from organic semiconducting materials. These materials have the advantage of low cost, labor saving manufacturing requirements, and ease of installment in comparison to inorganic crystalline solar cells.

In this thesis we discuss the physics of organic photovoltaics, how it differs

from conventional semiconductors, and the limitations that these physical processes impose upon photovoltaic devices. We then explain the procedure for fabricating both bulk heterojunction and planar heterojunction organic solar cells in our lab. We present the experimental results of our devices and compare the performance of our devices with simulations. Finally, we conclude with suggestions for future work built upon the research conducted in this thesis.

1.1 A Brief History of Solar Cells

The photovoltaic effect was first discovered in 1839 by Edmund Becquerel. He observed that light on a silver coated platinum electrode immersed in electrolyte produced an electric current [2]. Forty years later, in 1876, William Adams and Richard Day began exploiting the photovoltaic properties of selenium by using two heated platinum contacts and supplying light to produce a current. Charles Fritt fabricated the first large area solar cell in 1894, by using a layer of selenium pressed between gold and another metal. Later, cells were made from copper-copper oxide thin films, lead sulphide, and thallium sulphide. However, scientists at the time were more interested in the photoconductivity of these materials rather than their photovoltaic properties. Real developments in photovoltaics did not come until the 1950's, when developments in silicon for solid state electronics allowed scientists to design a p-n junction that could convert sunlight much more efficiently [2].

The first silicon solar cell was reported in 1954 with an efficiency of 6 percent, six times higher than previous attempts. Efficiencies rose significantly over the next decade, although manufacturing costs remained prohibitively high. However, one cost effective use for these devices was space exploration. Consequently, silicon solar cells were widely developed in the 1950s and 60s

for space applications [2].

Silicon remains the foremost photovoltaic material, primarily due to the advances in silicon technology made by the microelectronics industry. However silicon photovoltaics are reaching their fundamental limit in cost-efficiency trade off, and scientists are investigating new materials to meet the demand for cheaper solar alternatives.

1.2 An Alternative to Silicon: Plastic Solar Cells

Currently, interest in polymer solar cells has skyrocketed due to the hope that these materials will offer a better, cheaper alternative to silicon. The science of polymer processing is very well developed, and researchers have suggested that one day photovoltaic devices could be manufactured using roll-to-roll processing techniques to print large sheets of inexpensive, flexible, devices. However, organic photovoltaics still have a long way to go to compete with their silicon counterparts. Commercialized silicon photovoltaics currently have efficiency levels around 25%, while the very best laboratory processed organic devices have maximum efficiencies of around 10%. This dramatic decrease in organic efficiency stems from the physics of organic materials.

In 1959, Kallmann and Pope first observed the photovoltaic effect in an organic material: a single crystal of anthracene. When sandwiched between two identical electrodes and illuminated from one side, electrons could be harvested. Kallmann postulated that different exciton dissociation mechanisms must occur at the light and dark electrodes [3]. This study did not directly lead to the invention of the organic solar cell, however, because the physics of photogeneration was not fully understood, and the device architectures limited the efficiency levels of these organic photovoltages to less than 0.1%. In 1986,

a major breakthrough occurred when Tang discovered that bringing a donor and acceptor layer together in one cell dramatically increased efficiencies to levels near 1% [4]. This led to further investigation into the operation of these now promising devices.

The physics behind unconventional amorphous semiconductors is fundamentally different from that of inorganic crystalline semiconductors. In inorganic photovoltaics (IPVs), electron-hole pairs are generated immediately upon light absorption throughout the bulk [5]. In contrast, light absorption in organic photovoltaics (OPVs) typically results in the production of bound, but somewhat mobile, excited states. These semi-mobile states must travel throughout the material (via diffusion) until reaching a heterojunction. A heterojunction is the junction between two materials: the "active layers" in the device. Here the exciton can disassociate into an electron and a hole. One side of the junction holds a "p-type" semiconductor that will readily accept an electron, and the other has an "n-type" semiconductor to accept the hole. Thus the heterojunction acts as a charge separation device. However, the device can only produce charges when excitons physically reach the junction.

This process puts several fundamental limits on heterojunction organic photovoltaic devices. One limitation is the relatively short distance than an exciton can diffuse before recombining compared to the characteristic length required to absorb a significant amount of light. The exciton diffusion length in typical molecular materials is a few tens of nanometers. Therefore only the excitons generated in the ten nanometers next to the heterojunction can contribute to the photocurrent. However, even though organic materials typically have better absorption than crystalline semiconductors, hundreds of nanometers are still required for good optical absorption depth [2]. This problem is typically handled using the method of a bulk heterojunction. The two materials (p-type and n-type) are mixed together in solution. Generally, this solution

is then deposited via spin-coating or drop-casting. The first bulk heterojunction organic solar cells were reported by Yu, et al, in 1995 [6]. To date, bulk heterojunctions are the most successful method of fabricating organic photovoltaic devices [7]. Figure 1-1 illustrates the difference between a planar and bulk heterojunction device geometry.

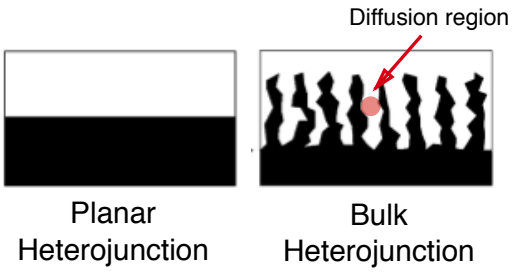

Figure 1-1: Illustration of the difference between planar and bulk heterojunctions

1.3 Advantages and Limitations of Bulk Heterojunctions

Much work has been done to optimize the efficiency of bulk heterojunction devices. An important characteristic is the morphology of the structure. Many studies have shown a correlation between morphology and efficiency in bulk heterojunction devices [7]. The uniformity of the heterojunction is influenced by many factors, including: the vapor pressure of the solvent [8, 9, 10], the rate of solvent removal [11, 12], the volume fractions of the components [9, 13, 14], the use of chemical additives [15], thermal annealing treatments [16], and solvent annealing [17].

Although the bulk heterojunction has produced the highest efficiency rates to date, its performance is intrinsically limited by some significant physical

constraints. Since the solution is processed in one simple step, it is difficult to control the formation of the interconnected pathways within the materials required for efficient and selective charge carrier transport to the appropriate collection electrodes. This inability to control the device's nanoscale properties can lead to increased losses in efficiency through charge carrier recombination and increased leakage current.

Because of these limitations, planar heterojunctions may offer a better alternative for fundamental studies because of the intrinsic control over the concentration and thickness of each layer. The option of synthesizing each layer independently means that growth parameters can be adjusted to optimize the efficiency of each layer. While bulk heterojunction photovoltaics have received a large amount of research attention in recent years, planar heterojunctions have been largely neglected due to the difficulty of successively depositing organic materials, combined with the widely held opinion that bulk heterojunctions offer unconditionally higher efficiencies. Although planar heterojunctions may not currently yield record setting efficiency levels, studying these devices will certainly allow us to better understand the organic-organic interface, ultimately allowing researchers to design solar cells that could combine the desirable properties of both the bulk and planar heterojunctions with new innovative device structures.

1.4 Our Work

In this thesis, we present an alternative to the bulk heterojunction device structure by demonstrating the success of a recently developed method of depositing successive layers of solution processed molecular materials. Our method employs stamping the electron acceptor layer, [6,6]-penyl-C61-butyric-acid-methyl-ester (PCBM), on top of a spin-coated hole acceptor layer, poly(3-

hexylthiophene-2,5-diyl) (P3HT). This fabrication process results in a planar heterojunction geometry. We successively experiment with variations in film thicknesses and seek to understand the physics of the heterojunction by testing the current-voltage properties of the devices.

We present our experimental results for P3HT/PCBM photovoltaic devices with both planar and bulk heterojunctions fabricated in our lab at Mount Holyoke College. We examine the properties of our devices by imaging the active layers with both an optical microscope and an atomic force microscope. We then present the device current-voltage characteristics for multiple device structures. The current-voltage characteristics of our planar heterojunction devices, while less efficient than their bulk heterojunction counterparts, offer an amazing result for the first attempt at a new device structure in our laboratory.

Organic materials behave differently than inorganics, and often the conventional equations for charge movement do not apply. We review the assumptions used to derive the equations for charge generation and transport in semiconductors and present a simplified analytical model for the operation of an organic solar cell. Our understanding must be fundamentally limited because of the approximations adopted. We utilize a modeling tool developed by Biswajit Ray, et. al at Purdue University and the Universidad Los Andes [18]. This model simulates the IV characteristics of a P3HT/PCBM bi-layer device through a four step charge generation process. The tool models a bi-layer device with a diffuse region of P3HT:PCBM in a 1 nm region at the heterojunction. Although the typical surface roughness of actual organic films mandates that this ideal scenario many not be practical, the simulation does give a general guideline for the efficiencies we can theoretically hope to achieve with our stamped devices.

To explore the physics of our devices in a more insightful way, we ran an

adapted Monte Carlo simulation that describes electrons and holes in the device as polarons, quasi particles that contain both a charge and the lattice disruptions that travel with the charge throughout the material. This description offers a more accurate representation of charge transport in organic materials because it can account for the energy interactions within the material. However, our analysis of the results of this model showed some serious discrepancy in the physical properties of the model. Because of this, we cannot compare the results of this model to our experimental results.

1.5 The Importance of the Heterojunction: A Fundamental Limitation on Efficiency

Many researchers agree that one of the fundamental limits to OPV efficiency is a tradeoff between open circuit voltage(V_{OC}) and short circuit current(I_{SC}) [19]. The output of the device is proportional to both V_{OC} and I_{SC}, and will be limited by a low contribution from either quantity. These quantities are defined as follows:

Open Circuit Voltage (V_{OC})**:** The maximum voltage produced by the device when no load is attached [20].

Short Circuit Current (I_{SC})**:** The current that flows from the circuit to ground when the output is shorted to ground.[20]

Together, the open circuit voltage and the short circuit current determine the power output for a device. Determining the origin of these quantities and possible connection to each other is crucial to maximizing efficiency. The conventional understanding of the relationship between V_{OC} and I_{SC} is shown by the image in Figure 1-2 illustrating two devices with material combinations of differing energy bandgaps. The energy level offset between the highest

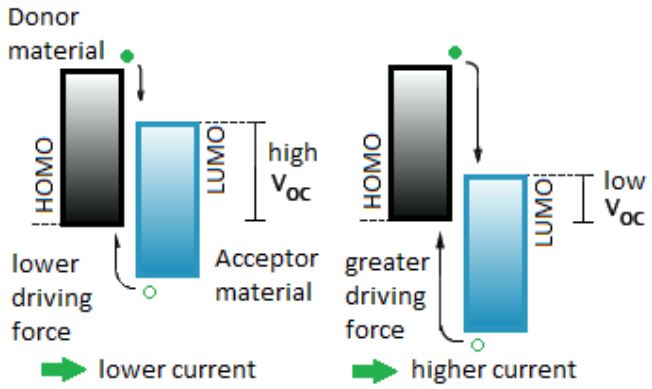

Figure 1-2: Energy diagram illustration of the tradeoff between open circuit voltage and short circuit current.

occupied molecular orbital (HOMO) in the donor material and the lowest unoccupied molecular orbital(LUMO) in the acceptor material is called the interfacial bandgap or the HOMO-LUMO offset. A device with a small interfacial bandgap is expected to produce a large I_{SC} because a photo-excited electron at the heterojunction experiences a larger driving force across the junction. However the size of the interfacial gap dictates that V_{OC} will be low for this system. Conversely, a donor-acceptor heterojunction with a large interfacial gap is expected to produce a low I_{SC} and high V_{OC}. If this model is correct, the tradeoff will ultimately limit the maximum efficiency that OPVs can reach. However in recent years, several studies have demonstrated V_{OC} values that break the upper bounds of this model [21, 10, 22]. These results are exciting, and demand a new explanation of the physics underlying open circuit voltage values in OPVs. In 2009, Vandewal et. al. published a report calculating the V_{OC} for fullerene polymer solar cells without directly relying on the optical bandgap of the materials or the devices HOMO-LUMO offset [23]. The paper instead demonstrates a relationship between V_{OC} and the interfacial emission rate. Emission at the interface detracts from the efficiency of the cell, and Vandewal's work suggests that quenching this emission could directly increase

V_{OC}, allowing scientists to design a cell that maximizes both V_{OC} and I_{SC}. Discovering how to do this would transform organic photovoltaics and open the door to commercial viability for this exciting new technology. Our work studies the physics at this critical junction in order to better understand how to design devices that suppress recombination, leading to higher open circuit voltages.

1.6 Previous Work

Although the stamping method of depositing active semiconductor layers was recently adapted for use in organic photovoltaics, several other research groups have used this method to attempt to make planar heterojunction devices. In 2008, Yim et. al. fabricated bi-layer P3HT/PCBM devices with a stamping procedure that employed the use of a sacrificial intermediate layer and only used the PDMS stamp for transfer from the original substrate to the P3HT film [24]. These authors found that the bilayer devices produced short circuit currents and open circuit voltages comparable to their bulk heterojunction counterparts. They studied a range of thicknesses, with the most successful device made from a ratio of 70nm P3HT/70nm PCBM. According to their report, they did not anneal their devices, but still achieved power conversion efficiencies near 1.7% with a reported short circuit current density of 7.6mA/cm^2 and V_{OC} of 0.6V. However, the fill factor of their devices was low, with the IV curve demonstrating high series resistance and high leakage currents. Also in 2008, Ferenczi et. al. performed a direct transfer printing process to fabricate P3HT/PCBM bilayer devices that yielded significantly lower efficiency levels for unannealled devices (J_{SC}=0.6mA/cm^2, V_{OC}=0.25V, power conversion efficiency of 0.05%) [25]. However, after thermal annealment treatments these efficiencies dramatically increased (J_{SC}=4.5mA/cm^2, V_{OC}=0.7V). In the

paper, the authors attribute this increase in efficiency to intermixing of the layers of P3HT and PCBM. They also note that the total thickness of their devices decreased after annealing, indicating that better contact between the layers of the device after annealing treatments could also be leading to higher efficiencies.

Interestingly, the results of Yim et al. contradict the widely held theory that excitons can only diffuse within a region of approximately 20 nanometers of depth, requiring the use of a bulk heterojunction. Yim's results invalidate the bulk heterojunction requirement and suggest that some new physics is required to explain his results. In response, Wang et. al published a study in 2010 investigating the morphology of stamp transfer fabricated devices [26]. These researchers used Auger spectroscopy to study devices made in this manner and found that the PCBM top layer was unexpectedly well blended with the P3HT bottom layer. According to this work, the supposed reason for this mixing effect was residual solvent on the P3HT film surface when the PCBM film was transfered. Wang concluded that the method of stamp transfer printing could be used as a procedure for preparing concentration graded bulk heterojunction films.

Another notable study about bilayer devices was by Ayzner et. al., in 2009. This group used orthogonal solvents for P3HT and PCBM to successively spin-coat the active layers of the device [27]. The group found similar enhancements to efficiency levels after thermal annealment treatments as Ferenczi et. al. Interestingly, the optimal ratio found between P3HT and PCBM layer thickness by this group was 4:1, a dramatic difference from the results of Yim et. al. In 2010, Casalegno et. al. published a report of a Monte-Carlo course grained simulation that suggests an alternative solution to the high efficiencies found by Yim and Ayzner [28]. According to Casalegno, the exciton diffusion length of the P3HT may be higher than previously thought.

This would concur with result by Ayzner indicating that the most important property of the device is the ratio of the thicknesses of active layers, and not merely the raw thicknesses of the layers.

As a result of this controversy, there is still much work needed to verify which solution, if any, is the correct explanation of the unexpectedly high efficiencies found in planar devices by a number of researchers. We have attempted the fabrication and simulation of a planar heterojunction device structure with the goal of extracting a better picture of the physics that is happening inside these devices.

1.7 Conclusion

In the next chapter, we present the basic theory behind charge generation and movement in organic materials, and the device physics of organic photovoltaics. We derive analytical expressions for the primary contributing mechanisms of operation in solar cells. The chapter concludes with a detailed summary of the desirable attributes in an ideal organic photovoltaic device. In chapter 3, we cover the fabrication methods employed to make our devices. We explain some of the challenges of working with organic thin films and present a summary of our work with these materials.

Chapter 4 contains the measured current-voltage characteristics of our bulk heterojunction and planar bi-layer devices, and a comparison of these results with simulations. The current-voltage plots are displayed, and we point out the key regions of interest and how these relate to the physics at the heterojunction of our devices. We next present the results of our analytical simulations for bi layer devices. These simulations demonstrate where the theoretical charge transport mechanisms limit the generation of photocurrent in the bi-layer device structure, particularly when the active layer of P3HT is thicker

than the exciton diffusion length used in the model. We use this model to further analyze the results of our experiments. Next, we present the results of a molecular scale monte carlo simulation for charge movement within organic materials. We perform a preliminary analysis on the results of this model, and find physical inconsistencies that prevent us from comparing these results to our experimental work.

In the final chapter, we summarize the findings of this thesis, and present plans for future work built upon the results outlined here.

Chapter 2

Device Physics

This chapter explains the physical quantities and basic physical processes responsible for converting sunlight into electrical power. In the previous chapter we explained the open-circuit voltage and short circuit current, and how these quantities determine the power output for a device. In general, the efficiency at which solar cells convert light into electricity can be described by five independent quantities that depend on both the material properties and the device physics of operation. These are: the absorption of the active layer, the efficiency of photon to electron conversion, the bandgap E_g of the active absorbing material(s), the maximum voltage generated by a device, and the internal resistive properties of the device. These fundamental properties are discussed and the processes underlying them are explained. We then conclude with the fundamental limits that apply to the efficiency of solar cells and suggest the ideal solar cell to optimize all of the constraints in the system.

2.1 Photon Absorption

When photons of a given energy contact the active material, they interact with molecules of that material over a distance x with a probability A_0. This means

that the Intensity I_0 of the light in the material then must decrease by a factor of $(1 - A_0)$ as it passes through the first layer of molecules, and then again by the same factor as it passes through the next layer, and so on throughout the device. The total Intensity then, can be written as a function of position:

$$I(x) = I_0(1 - A_0)^{\frac{x}{\Delta x}} \tag{2.1}$$

where $x = (i) \times \Delta x$ and Δx is the thickness of the ith layer of molecules. This expression can be re-written as

$$I(x) = Ie^{-\alpha x} \tag{2.2}$$

where

$$\alpha = \frac{-ln(1 - A_0)}{\Delta x}$$

This gives us the quantity α, an intrinsic property of the material. Since more photons are absorbed with increasing thickness, the ideal thickness of the active layer will be such that a significant portion of the photons are absorbed. A notable advantage to molecular materials is that they typically have much higher absorption coefficients than materials with long range order, such as crystalline semiconductors. This means that photovoltaic devices made from organics can be much thinner than their silicon counterparts, and still absorb a significant fraction of the incident light. Figure 2-1 illustrates the effect of the thickness of a film on the amount of photons reaching the edge of a material. In general, thicknesses should be on the order of $1/\alpha$, which is sufficient to absorb 63 percent of incident photons [21].

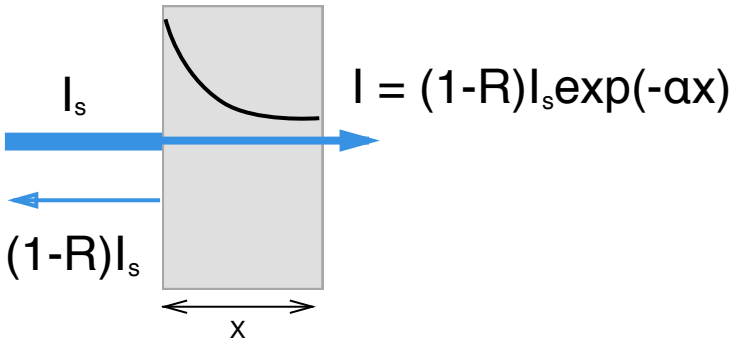

Figure 2-1: Illustration of the effect of the thickness of a material on the amount of photons penetrating the material I_s represents the intensity of the incident light, (1-R)I_s the reflected light, and the black curve the intensity of light in the material.

2.2 Efficient Photon to Electron Conversion

When a photon is absorbed by the material, it generates an electron-hole pair, called an exciton, which can potentially dissociate at the heterojunction of the two active layers of the material and generate free carriers that travel to the electrodes, producing photocurrent. Figure 2-2 illustrates the basic structure and fundamental process of a solar cell. This entire process can be quantified

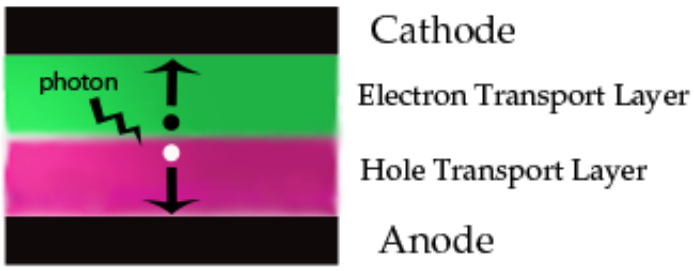

Figure 2-2: Cross section of a solar cell showing an electron hole pair generated at the interface and subsequent movement to the anode/cathode of the device

by an expression called the Quantum Efficiency.

External Quantum Efficiency (EQE): The probability that one photon at a single energy level produces one electron that arrives at the electrodes of the device

Mathematically this is described as:

$$EQE(E) = \frac{Generated\,electrons}{Incident\,photons\,@\,E_k} \tag{2.3}$$

This quantity depends on many different factors, and particularly can be broken into both the absorption of the device, and the rate at which absorbed carriers are converted into electrons. This last quantity is given a special title:

Internal Quantum Efficiency (IQE): The probability that one absorbed photon produces one electron arriving at the electrodes of the device.

We can write this as:

$$IQE(E) = \frac{Generated\,electrons}{Absorbed\,photons\,@\,E} \tag{2.4}$$

So that EQE can be now rewritten as:

$$EQE(E) = IQE\ x\ Absorption\,@\,E_v \tag{2.5}$$

EQE can theoretically reach 100 percent, but factors such as reflection, absorption, and transport losses typically lower this conversion to around 80 percent.

In order for one photon of light to produce one electron at the electrodes of the device, there are four key process that it must undergo. These processes are illustrated in Figure 2-3. The first process is the absorption of a photon in the material, generating a bound electron hole pair, an exciton. The second step is the movement of the exciton to the heterojunction of the two active

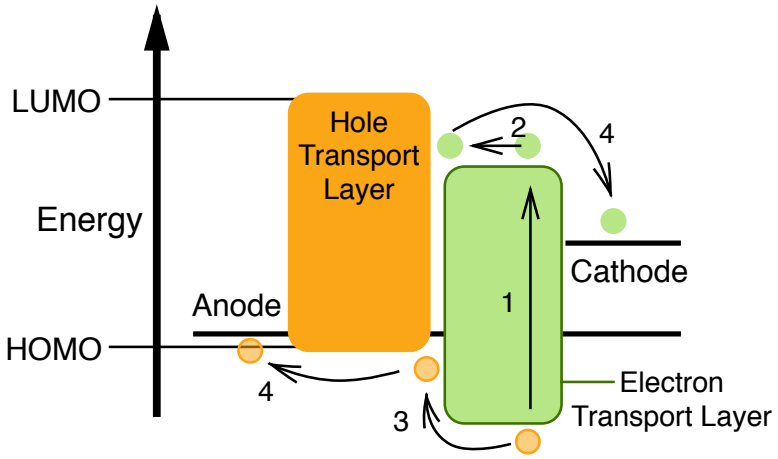

Figure 2-3: Illustration of charge generation and transfer processes in an organic solar cell: (1) Exciton generation (2) Exciton movement across the device (3) Exciton dissociation into an electron and a hole (4) Charge movement across the device to the electrodes

layers in the material. This process is governed by exciton diffusion which will we further study in section 2.2. When the exciton reaches the heterojunction, the third process is the dissociation of the electron-hole pair across the interface. Either the electron or the hole will charge transfer across the interface depending on the energy level alignment of the two materials. The resulting pair is still bound across the interface, however this bond is much weaker. The electron and hole pair separates and free carriers are formed. The final process is the movement of the free carriers (separated electrons and holes) across the material to the electrodes. The processes relevant to IQE will now be discussed, beginning with exciton movement after the initial photoexcitation.

2.3 Exciton Movement

Many researchers have studied the specifics of how excitons build up and move throughout a film of organic materials [29]. The motion is governed by several key parameters. Each specific material has a unique exciton diffusion

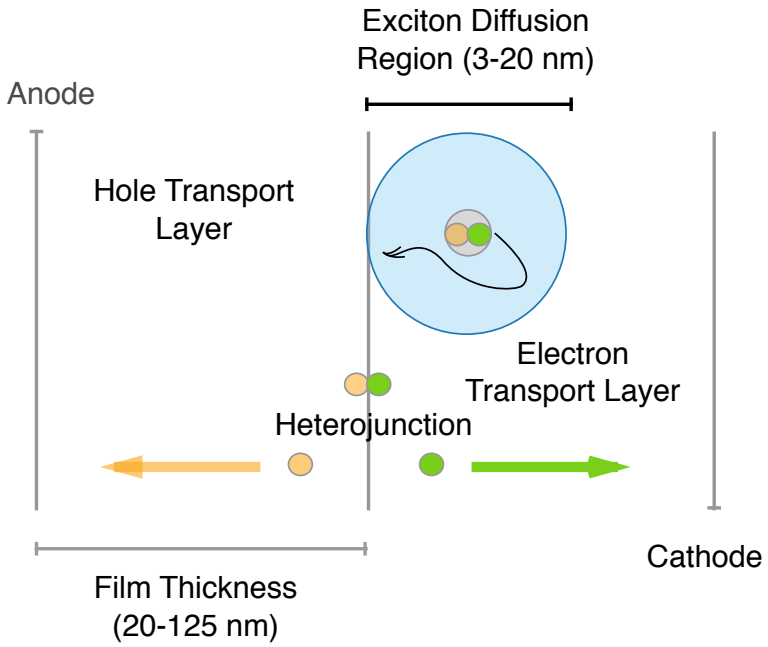

Figure 2-4: Charge generation process via the production of excitons for organic solar cells

length, the length that a single exciton can travel before being re-absorbed into the bulk. This parameter can be determined experimentally, and we can generally determine the rate at which this process should occur theoretically as well. Figure 2-4 illustrates the process by which charge is generated for excitonic solar cells. The theoretical treatment of this process follows from the understanding of an exciton as a charge neutral species, capable of movement between molecular sites independent of most external electric fields [21]. There are two important physical processes that account for the movement of this exciton through the bulk. The first is direct charge transfer, called Dexter transfer. This rate of charge transfer can be specified by the wavefunction overlap of the two molecules. The expression for this is just:

$$r = r_0 e^{\gamma \Delta x} \tag{2.6}$$

With r_0 the wavefunction overlap, γ the fall off of the overlap with distance and Δx the distance between states. This clearly can only take place at very small length scales, where the wavefunction overlap term is large. The second method of exciton movement is called Forster transfer, and describes long range energy coupling. This transfer rate is described by:

$$r = \frac{1}{\tau_{rad}}(\frac{R_F}{\Delta x})^6 \tag{2.7}$$

The key term is R_F, the Forster radius, which is typically on the order of 3-8nm for most molecular systems [21]. τ_{rad} is the radiative lifetime of the exciton.

These two equations are the basis for describing charge pair movement in molecular semiconducting films. Some groups have investigated further by modeling energetic states in molecular systems, disordered arrangement of molecules in a film, and inhomogeneity in molecular scale polarization [29, 30].

As stated earlier, excitons have no net charge and their movement is strictly determined by these rate equations which depend only on spatial location. The important factor in determining how likely excitons are to move towards the separating interface is the concentration gradient of the excitons in the material. Once this distribution is known, we can calculate how many excitons ultimately reach the heterojunction in the device and thus determine the internal quantum efficiency. We neglect exciton-exciton interactions since these interactions can be shown to be negligible for solar intensity levels [21].

The description of this carrier concentration is the steady state exciton diffusion equation, given by:

$$0 = L_{ED}\frac{d^2 p_j}{dx^2} - p_j + \tau G_j \tag{2.8}$$

Where p_j is the number of excitons, L_{ED} is the exciton diffusion length for

the material, τ the exciton lifetime and G the generation rate for excitons [21]. This equation can be solved independently for varying film thicknesses to understand the carrier concentration dependence upon device thickness.

To harvest the greatest number of excitons, the ideal material thickness is typically on the order of the diffusion length of the material, L_{ED}. The actual solution of the carrier concentration at this thickness can often become difficult to solve, because of additional constraints. This has lead to much theoretical work done utilizing Monte Carlo modeling to describe the exact distribution [29, 31].

2.4 Movement of Free Carriers

Once free electrons and holes have been generated at the interface, they must travel across the two separate materials (n-type and p-type respectively) to reach the electrodes. This movement can be approximated by the well understood transport equations used in crystalline semiconductors [2].

$$\frac{dE}{dx} = \frac{q}{\epsilon}(p - n) \qquad (Gauss' \, Law) \tag{2.9}$$

$$J_e = qn\mu_e E + qD_e \frac{dn}{dx} \qquad (Electron \, current \, equation) \tag{2.10}$$

$$\frac{dn}{dt} = G - R + \frac{1}{q}\frac{dJ_e}{dx} \qquad (Electron \, continuity \, equation) \tag{2.11}$$

Since electrons have charge, the electric field in the device will now contribute to the movement, this is the first term in the electron current equation and is called the drift current. The equations must also account for diffusion, this is the second term in the electron current equation. Together the expression is called the drift-diffusion equation. Since these equations were initially derived for use in crystalline semiconductors, it is worthwhile to look at the

assumptions that they are based on and consider if exceptions must be made for molecular materials. These are [2],

- Electron and hole concentrations independently form in a thermal equilibrium and have a characteristic Fermi level and temperature

This is one of the defining properties of crystalline semiconductors, however low-mobility materials will deviate from this due to the long time scale of carrier interactions between molecules in the bulk. The time frame for the Fermi level of the electrons in one side of the material to reach equilibrium with the Fermi level of the molecules at the other side of the device might be large.

- Electron and hole temperatures are always the same as the lattice temperature

This will fail when electrons or holes gain extra kinetic energy; for example through acceleration through high electric fields or, in our case, when the bound electron-hole pair moves across the heterojunction. This dictates that the drift-diffusion equations do not apply to charge movement at the heterojunction.

- Interactions with the lattice are more frequent than generation, recombination or trapping events. This dictates the relaxation time approximation used in the expression.

This is still a reasonable approximation for organic molecules, however does not hold at an abrupt boundary between two different semiconductors, in our case the heterojunction.

- Electron and hole states can be described by a quantum number K

This assumption does fail for amorphous materials. The consequence is that carrier mobilities cannot be rigorously determined by traditional methods.

However empirical expressions for mobilities can be used instead. Typically carrier mobilities for molecular materials will be much lower than those for crystalline semiconductors

- The Boltzmann approximation ($E_c - E_{Fn} >> k_BT$ and $E_{Fp} - E_v >> k_BT$)

This assumption only fails for degenerate semiconductors, which are so highly doped that they begin to behave like metals. This is not an issue for molecular materials.

- Compositional invariance

This assumption greatly simplifies the equations by assuming that there is only one electrostatic field present in the material. For the purposes of the calculations in this thesis, we will maintain this assumption, although it is almost certainly not actually the case because molecular level electrostatic interactions are involved in charge transfer.

Now that we have established the legitimate application of the drift-diffusion equations for molecular materials, we can examine how these equations dictate device performance.

Several studies have been done to experimentally determine whether the drift or diffusion term will dominate for different device structures. Ramsdale et al. measured V_{OC} in a polymer bi-layer device for a range of cathode and anode work functions, which would vary the electric field within the device significantly, and thus the contribution to current from the drift term, and found that the total collection of electrons at the electrodes did not change significantly, indicating that diffusion dominated [32]. For bulk heterojunctions, Mihailetchi et al. observed that the photocurrent did decrease when the work function offset was changed, but this change in offset was much smaller than expected from a purely drift driven offset [33]. These studies indicate

that the diffusion term plays a larger role than the drift term for molecular semiconductors.

The studies by Ramsdale on bi-layer device charge transport indicate a purely diffusion driven current, and the studies by Mihailetchi demonstrate a similarly diffusion driven current but with some contribution from the drift term. This highlights an important difference between planar and bulk heterojunction charge transport. Diffusion plays a much larger role in planar heterojunctions than in bulk heterojunctions, therefore free carrier charge transport is yet another variable that changes significantly when the heterojunction geometry is altered.

2.5 Impact of the Semiconductor's Bandgap

The bandgap E_g of the active layer semiconductor(s) controls two important factors in the solar cell: the part of the solar spectrum absorbed (directly), and the open circuit voltage (indirectly). Incident photons at a lower energy level than the semiconductor's optical bandgap will be unable to generate excitons. However, photons whose energy level is greater than that of the energy level bandgap of the material will waste all of their excess energy through thermal relaxation. An absorbed photon whose energy level is $E >> E_g$ will generate the same exciton that a photon with energy $E = E_g$. In this way, photogeneration is determined not by photon energy density but by incident photon flux. Clearly the optimal bandgap should not be either too high or too low. In 1980, Henry calculated the theoretical optimal bandgap for a solar cell operating under typical solar illumination [34]. He calculated the total number of photons with energy levels above E_g by integrating over the solar spectrum curve, which is roughly a blackbody curve with peak radiation at 5777°C. He then found the energy produced by any solar cell at a given bandgap by mul-

tiplying this number by (E_g - 0.4eV). The 0.4eV is subtracted due to thermal excitations set by temperature. The bandgap that will generate the maximal energy found in this way is 1.4eV [34]. As a result, most materials studied for solar cell applications have a bandgap in this range. The bandgap for P3HT is 2eV and PCBM is 2.4eV.

2.6 Open-Circuit Voltage

The energy level bandgap of the active layer semiconductors also contributes to the open circuit voltage generation in a solar cell. There has been considerable debate on the origin of open circuit voltage in molecular photovoltaic systems, however many researchers agree that this quantity depends on the interfacial gap between the active layers in a solar cell as illustrated in Figure 1. In the conventional understanding, increasing the interfacial bandgap increases the V_{OC} of a device, but decreases the short circuit current. In order to fully understand how this works, we will briefly discuss the detailed-balance model, originally described by Queisser and Shockley in 1961 [35]. Our explanation is simplified and follows the description by Alexi Arango, 2010 in [21].

As light hits the semiconductor layers in the solar cell, charge carriers are produced at a generation rate G, producing a photocurrent

$$J_{photo}(I) = q\,G(I)d \tag{2.12}$$

where d is the thickness of the semiconductor of layer and I is the intensity of the incident photons. If a bias is applied to the electrodes, carriers are injected from the electrodes, raising the carrier concentration and overall recombination rate. The primary mechanism for current flow is then the radiative recombination:

$$R = Bnp \tag{2.13}$$

where the B is the bi-molecular recombination constant, dependent on the materials in the solar cell. n and p are the electron and hole concentrations in the solar cell, given by the Boltzmann approximation:

$$n = N_c e^{(E_c - E_{Fn})/k_B T} \tag{2.14}$$

$$p = N_v e^{(E_{Fp} - E_v)/k_B T} \tag{2.15}$$

Where N_c is the density of states in the conduction band, N_v the density of states in the valence band, E_c and E_v th energy level for the conduction and valence bands,E_{Fn} the Fermi level for electrons, and E_{Fp} the Fermi level for holes. In this situation, the dark current is:

$$J_{dark}(V) = qR(V)d - qG_0 d \tag{2.16}$$

where G_0 is the thermal generation rate and R(V) is the voltage-dependent radiative recombination rate. Even in the dark, under no bias, thermally excited carriers produce a small amount of current. Under illumination,

$$J_{light}(I, V) = J_{dark}(V) - J_{photo}(I) \tag{2.17}$$

And thus the total current is:

$$J_{light}(I, V) = q\,R(V)\,d - qG_0 d - qG(I) \tag{2.18}$$

With $J_{light} = 0$, the relationship between generation and recombination at V_{OC} is then

$$R(V_{OC}) = G_0 + G(I) \tag{2.19}$$

showing that the recombination rate is determined by the total generation rate. This result means that at a given intensity and fixed temperature, V_{OC}

depends exclusively upon J_{dark} but not J_{photo}. V_{OC} can be completely determined by testing the operation of the solar cell under dark conditions, and is not associated with the photogeneration process in any way. Because of this, V_{OC} can be described as the point where the photocurrent generated by the semiconductor is fully consumed by recombination [21]. The equation governing V_{OC} can be obtained by considering the dependence of R on carrier concentration and voltage. In the Boltzmann approximation, carriers in the semiconductor recombine radiatively across the semiconductor bandgap at a rate of

$$R(V) = Bnp = BN_cN_ve^{-(E_c-E_v-E_{Fn}-E_{Fp})/k_BT} = KE^{-(E_g-qV)/k_BT} \tag{2.20}$$

using the fact that voltage is related to the Fermi levels in the semiconductor by $qV = E_{Fn} - E_{Fp}$ and that $K = BN_cN_v$ is a material constant. Now we just solve for V:

$$V = \frac{E_g}{q} - \frac{K_BT}{q} ln(\frac{K}{G_0 + G(I)}) \tag{2.21}$$

and using Equation (2.13), we have:

$$V_{OC} = \frac{E_g}{q} - \frac{k_BT}{q} ln(\frac{N_cN_v}{np}) \tag{2.22}$$

The second term will always be positive, and thus the maximum value for V_{OC} occurs at T=0.

For donor/acceptor heterojunction devices, the description of V_{OC} is very similar, but instead relies on N_c of the electron transport layer and N_v of the hole transport layer so that the equation is now:

$$V_{OC} = \frac{E_g}{q} - \frac{k_BT}{q} ln(\frac{N_{c,ETL}N_{v,HTL}}{np}) \tag{2.23}$$

with a maximum Voc again at T=0, equal to E_g/q.

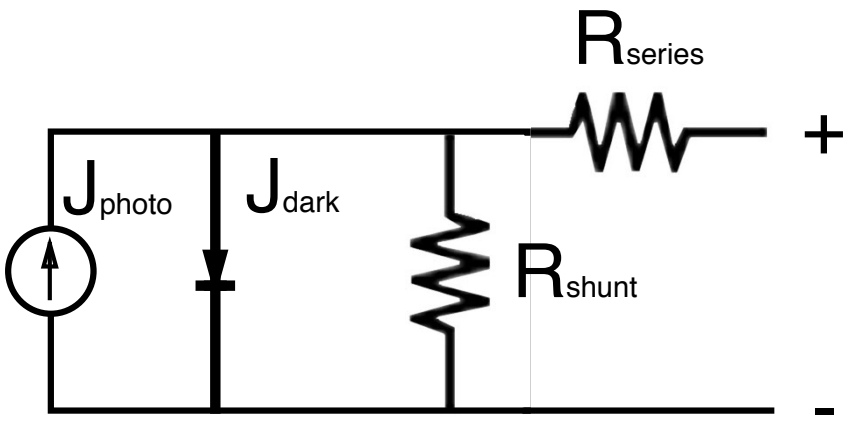

Figure 2-5: Circuit model for a solar cell under illumination with parasitic resistance and leakage current

2.7 Finding the Maximum Power: Fill Factor

The final factor limiting the efficiency of a photovoltaic device is the fill factor. This term contains information about parasitic resistances or non-idealities that cause the cell to function less efficiently. To understand these resistances and how they cause the solar cell's efficiency to decrease, we can look at the circuit model of a photovoltaic device in Figure 2-5. The solar cell is a current source with a rectifying diode, so that it can only turn on under the right conditions. The shunt resistance, R_{sh} should be high, so that minimal leakage current can bypass the diode when the solar cell is reverse biased. This parameter typically reflects nonconformities in the film, undesired pathways that allow the hole transport layer to make contact with the cathode, or the electron transport layer to make contact with the anode. The series resistance R_s, should be low, because all generated photocurrent must pass through the series resistor in order to arrive at the electrodes of the device. Any voltage

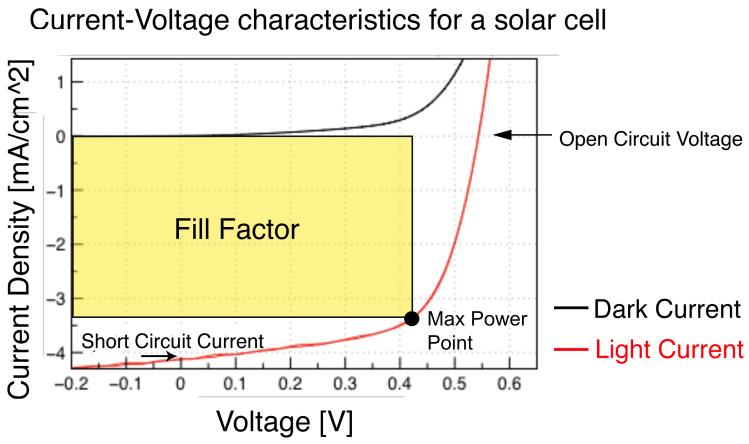

Figure 2-6: Current Voltage Characteristics of a solar cell under applied bias (dark current) and under illumination (light current)

dropped over this resistor is power loss from the solar cell. This parameter typically reflects charges lost when moving through the active layers of the device. A device made with too thick of an active layer will typically display high series resistance.

The Fill Factor of a solar cell represents the amount of total power output available from the device. On a current-voltage plot it is represented as the area inside of the I-V curve. Mathematically, it is described as:

$$FF = \frac{J_{mpp} V_{mpp}}{J_{SC} V_{OC}} \tag{2.24}$$

Where J_{mpp} and V_{mpp} are the current density and voltage at the maximum power output. Graphically, the Fill Factor is represented in Figure 2-6. A solar cell's power efficiency is defined as the ratio of electrical power produced to optical power incident on the device. This efficiency is:

$$\eta = \frac{Power\,Out}{Power\,In} = \frac{J_{SC}\,V_{OC}\,FF}{Power\ In} \tag{2.25}$$

where the Fill Factor should be maximized to produce the maximum efficiency

for the device.

2.8 Conclusion: The Ideal Solar Cell

With the operating principles of photovoltaic devices and the constraints of molecular semiconductors outlined in this chapter, we can now define the characteristics of an ideal, maximum power producing, organic solar cell. We want our devices to exhibit:

- High absorption in the active layers of the device $> 10^5\, cm^{-1}$
- High mobility in the the active layers of the device $> 10^2\, cm^2\, V^{-1}\, s^{-1}$
- Bandgaps of the active layers of the device that are near to the optimal bandgap in the detail-balance limit, 1.4 eV
- Low recombination rates at the heterojunction of the device
- Low series resistance and high shunt resistance

Devices with these characteristics, if possible, could alter the current-voltage tradeoff model discussed in our introduction and be used for large scale applications with efficiency levels competitive with those of silicon photovoltaics.

Chapter 3

Fabrication and Characterization

We have introduced the motivation behind designing efficient organic photovoltaic devices and the current understanding of the theoretical principles underlying molecular donor/acceptor devices. Furthermore, we have articulated the basic desirable quantities that an ideal organic photovoltaic device will exhibit. With this goal, we need a methodical approach to experimentation that allows us to fine tune the properties of our devices to achieve these quantities. In this chapter, we describe the specific practices used to fabricate the devices used in this thesis. We begin with a pre-patterned sample and deposit successive layers of the device onto the substrate using a combination of spin-coating, stamping, annealing, and thermal evaporation techniques. The multitude of variations possible in the application of these techniques allows us many options for optimizing parameters in our devices. Our devices are then characterized under standard conditions, and we report the performance of our cells as a function of applied bias.

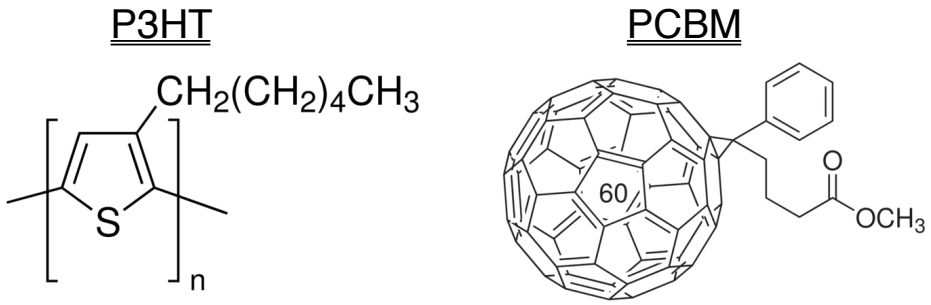

Figure 3-1: Chemical structure of P3HT and PCBM molecules

3.1 Our Materials

In this work we use two reasonably well studied polymers to form the active layers in our devices. The two materials are: p-type active layer poly(3-hexylthiophene-2,5-diyl) (P3HT) in conjunction with our n-type material, [6,6]-penyl-C61-butyric-acid-methyl-ester (PCBM). The chemical structure of these two materials is shown in Figure 3-1. These materials can be mixed together in a solution with mutual solvent 1,2-Dichlorobenzene (DCB) at various different concentrations, and deposited in a single step process to form a bulk heterojunction. Alternatively, the materials can be deposited successively to form a planar heterojunction using a combination of techniques. In the next section we present methods for fabricating bilayer devices using a successive spin-coating and stamping procedure. The solvent, orthodichlorobenzene is an organic compound that is poorly soluble in water, but miscible with most organic solvents. It is a derivative of benzene and has adjacent chlorine centers as shown in Figure 3-2. Another important part of our device is the bottom contact electrode, the anode. We begin with a glass substrate coated with Indium tin oxide (ITO). Indium Tin Oxide is a commonly used as a metal contact layer for photovoltaics and has a chemical structure of In_2O_3/SnO_2 We then deposit a layer of poly(3,4-ethylenedioxythiophene)poly(styrenesulfonate)

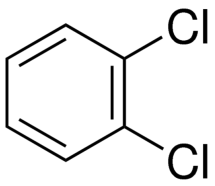

Figure 3-2: Chemical structure of orthodichlorobenzene

(PEDOT:PSS) on top of the ITO electrode. PEDOT:PSS is used to facilitate the hole transfer between the active layer and the ITO electrode. This material has the ability to smooth the surface roughness of the contact between the active layer and the electrode, and its work function, at 5.1eV, lies between the work function of ITO (4.7eV) and the HOMO level of most p-type organic semiconductors. These properties have led to PEDOT's use as the polymer anode in many organic light emitting diode(OLED) and OPV applications [36].

After deposition of the active layer, we deposit the top contacts via thermal evaporation. The materials used for the top contacts (cathode) are calcium (Ca) and silver (Ag). The calcium forms the cathode and the silver facilitates electron transfer.

The solar cells are then ready to be tested by our characterization procedure. The entire fabrication and characterization process is completed under a nitrogen atmosphere in successively connected glovebox chambers to prevent degradation of our samples via oxidation.

3.2 Device Structure

The structure of our devices is illustrated by Figure 3-3. Each layer of the solar cell is deposited in the multilayer pattern illustrated by Figure 3-4 [21]. This pattern design allows each sample to contain ten separately testable devices. The small device area dictates very small material waste in order to minimize

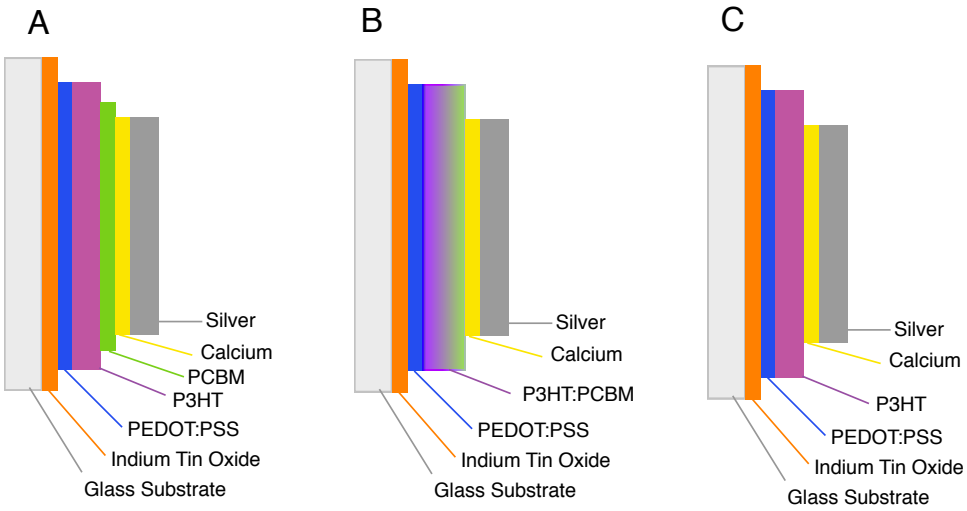

Figure 3-3: Device Structure used in this thesis for the A) Planar Heterojunction Devices B) Bulk Heterojunction Devices and C) Control device structure

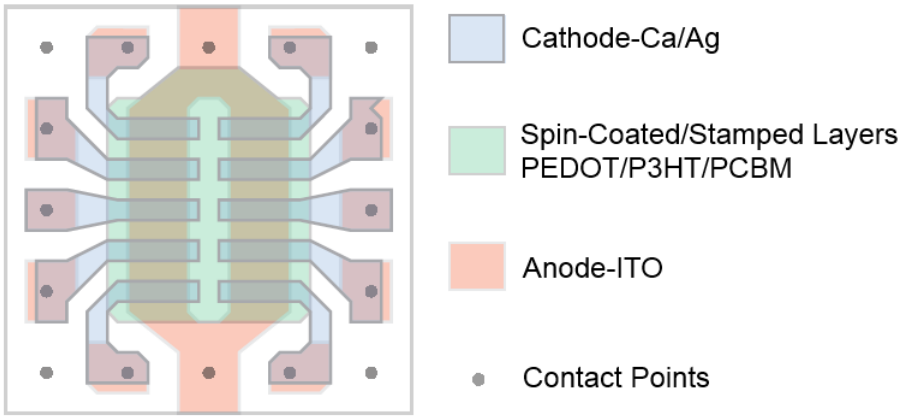

Figure 3-4: Top view of device structure Image credit: Alexi Arango

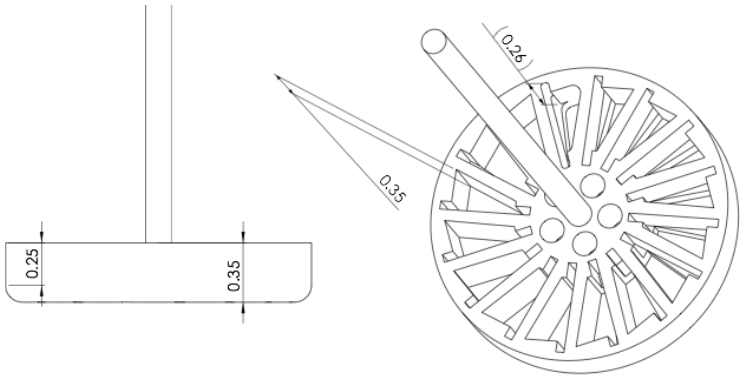

Figure 3-5: Substrate Dipper used for cleaning multiple samples

the cost of testing many different methods, device thicknesses and solvent concentrations.

3.3 Substrate Preparation

These substrates are sequentially cleaned by ultrasonication in micro-90, deionized water, acetone and isopropanol alcohol (IPA) for 5 minutes each. The samples are then transfered to a nitrogen atmosphere glovebox while still in the IPA solution, where they are then removed and dried via nitrogen stream and placed in individual floroware cases for future use. To expedite this process, we specifically designed a tool for cleaning up to 16 samples at a time with minimal waste. This tool was designed in SolidWorks and fabricated by Thomas Liimatainen of Mount Holyoke College. Figure 3-5 gives the design specifications for this part.

3.4 Deposition of PEDOT:PSS

A very thin film of PEDOT:PSS is deposited on top of the ITO anode by spin coating. The sample is placed on a substrate stand, the stand pulls vacuum

onto the bottom side of the sample so that it cannot move, an excess amount of material is deposited onto the sample, and then the sample is rotated at a high speed. In this way, excess material is removed via centrifugal force, and ultra thin films (down to less than 10nm in thickness) can be deposited in a simple manner. For our samples, 50μL of PEDOT:PSS is deposited onto the substrate and spun at a rate 5000rpm for a duration of 60 seconds. The samples are then placed on a hot plate and annealed at 190°C for 5 minutes. AFM measurements of these films determined the thickness to be between 12.5nm and 16.5nm.

3.5 Active Layer Deposition

We have fabricated two separate kinds of solar cells in this thesis: bulk heterojunction devices and planar heterojunction devices. These two kinds of devices are fabricated identically, except for the methods used for the deposition of the active layer.

3.5.1 Bulk Heterojunction Active Layer Deposition

P3HT (Poly(3-hexylthiophene)-regio-regular) and PCBM ([6,6]-Phenyl C61 butyric acid methyl ester) stock solutions are obtained from Solaris Chem Inc. with purity levels of 99.5%. A solution is then formed by mixing the P3HT:PCBM in a 1:1 ratio and dissolving into a solution of dichlorobenzene in a ratio of 40mg/mL. Anhydrous dichlorobenzene is obtained from sigma-aldrich with a purity level of 99%. A magnetic spin tab was inserted and the solution was then left to stir overnight on a magnetic stir plate.

Next the substrate is placed on the spin coater and 35μL of P3HT:PCBM is deposited onto the substrate and spun at rates of 600-800 rpm for a duration of 60 seconds. The samples are then placed on a hot plate and annealed at

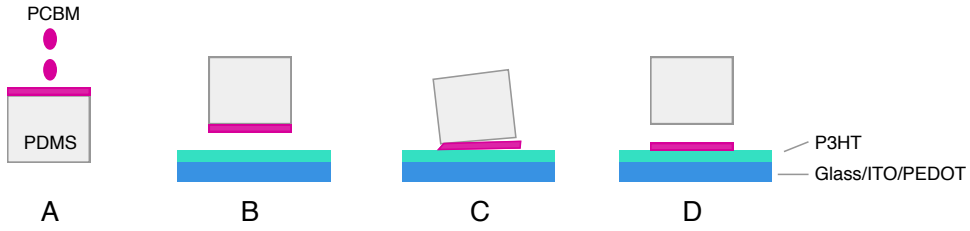

Figure 3-6: Procedure for stamping PCBM on top of a film of P3HT. A) A layer of PCBM is spin-coated on top of the PDMS stamp B) The stamp is held above the sample with P3HT film pre-spun C) The stamp is firmly pressed against the P3HT film D) The stamp is removed

150°C for a duration of 10 minutes. We experimented with several different thicknesses in the P3HT:PCBM films by varying the spin rate for deposition.

3.5.2 Planar Heterojunction Active Layer Deposition

The successive deposition of P3HT and PCBM active layers in a planar heterojunction structure has proven to be a very difficult feat to achieve. Since both P3HT and PCBM are dissolvable in mutual solvents, we cannot simply spin coat successive layers of each material without compromising the planar structure of the heterojunction. We employ a low pressure stamping technique to successively deposit the PCBM active layer on top of a spin-coated active layer of P3HT. The procedure for this method is shown in Figure 3-6. We dilute the P3HT in a solution of dichlorobenze at a concentration of 43mg/mL. We then deposit 35μL of the P3HT solution onto the sample and spin films at varying rates of 600, 700, 800, 1500, 2000, 2500, and 3000 rpm. The films spun at lower speeds were thick and somewhat clumpy, therefore devices were not made from these films, however images were taken. Higher spin speeds generated layers of P3HT that appeared to be reasonable thicknesses with some variations on morphology visible in the images taken with a optical microscope. Optical microscope images of several films are displayed in Figure

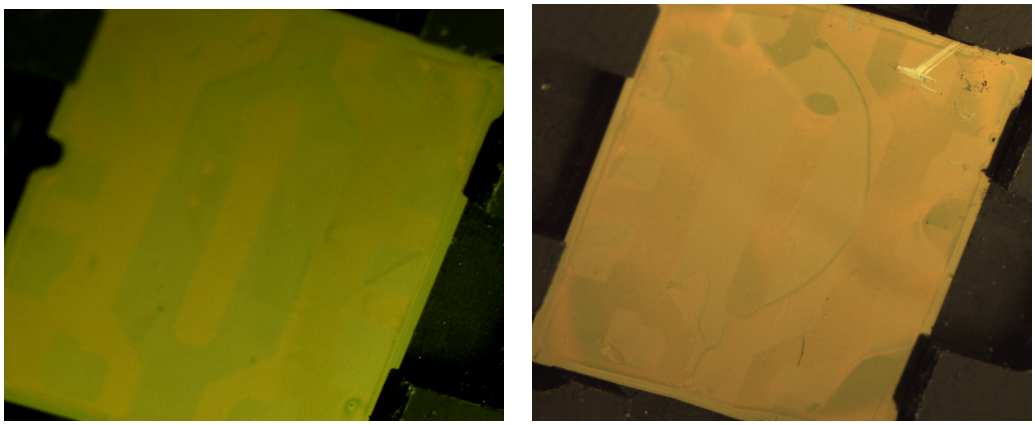

(A) (B)

Figure 3-7: Images of Pristine P3HT Films spun at varying speeds taken with an optical microscope. (A) Film spun at 1500rpm and (B) 2000rpm

3-7. The difference in color between the images is a result of variations in the hue setting on the microscope taking the images and does not reflect any variations the actual color of the films.

The next step is to apply a layer of PCBM without modifying the pre-existing layer of P3HT. We attempt this process via a simple stamping technique illustrated in Figure 3-6. We use elastomeric stamps made from polydimethylsiloxane (PDMS). The PDMS is cured at 60C for two hours to form an optically smooth conformable surface and then sectioned into 1 cm^2 stamps. The standard operating procedure (SOP) for making these stamps is listed under Appendix A. These stamps are cleaned by depositing 35μL of dichlorobenzene spun at a rate of 600 rpm for 60 seconds with a final spin-off cycle of 2500rpm for 3 seconds.

We dilute the PCBM in a solution of dichlorobenzene at a concentration of 50mg/mL. Next we deposit 35μL of this PCBM solution onto the stamps. The stamp is spun at a rate of 600 rpm for 60 seconds with a final spin-off cycle of 2500rpm. The coated stamp is pressed against the device stack, making contact first at one edge and then the entire device, to minimize air pockets

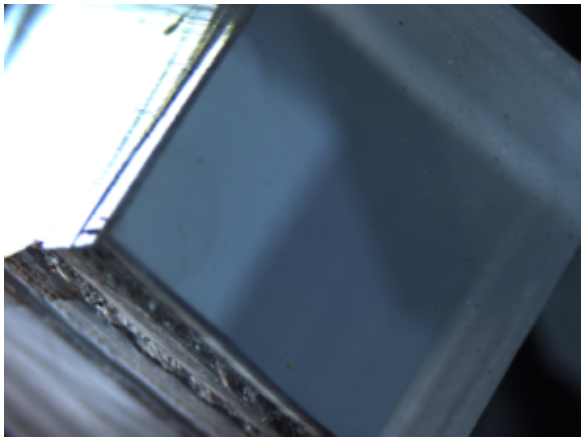

Figure 3-8: Optical microscope image of PDMS stamp with PCBM film before stamp deposition

between the active layers. The stamp and substrate are then immediately separated, leaving the PCBM film adhered to the P3HT. An image of the PDMS stamp with a PCBM film on top is shown in Figure 3-8. The Standard Operating Procedure (SOP) for deposition of the active layers of these bi-layer devices is listed under Appendix A in this thesis.

3.6 Deposition of Top Contact Electrodes

The top contact electrodes are deposited by the use of a thermal evaporator. The evaporator used in our laboratory was custom made to fit underneath our gloveboxes in an innovative miniaturized design. The samples can be easily loaded and unloaded from inside of the gloveboxes so that devices are not exposed to oxygen degradation and pump-down times remain short. However, deposition materials can be refilled from outside of the glovebox. A SolidWorks representation of the evaporator chamber is shown in Figure 3-9.

The samples are placed in a mask assembly that creates the patterned structure in Figure 3-4. The mask assembly can hold up to 16 devices at one

time and defines an array of ten patterned electrodes on each sample. Figure 3-10 shows a SolidWorks representation of the mask.The substrates are placed in a substrate holder that is then loaded into the evaporator on top of the shadow mask. The evaporator is then brought down under vacuum pressure of approximately $1.0x10^{-7}$ Torr. Once this pressure is achieved, the material to be deposited (which sits below the samples on a boat) is heated by sending a current through the material. As the current is increased, the material eventually begins to sublime, coating the walls of the chamber and the samples above. A quartz crystal monitor (QCM) is used to measure the thickness of the material as it is deposited. During the initial heating stage of the material, a shutter covers the samples so that no impure material is deposited on the samples. Once a steady rate of evaporation has been achieved (as detected by the QCM), the shutter is opened and material is deposited on the devices. We deposit 250nm of Calcium at a base pressure of $1x10^{-6}$ at a rate of 0.2nm/sec followed by a layer of Silver, 800nm thick, at the same base pressure and evaporation rate as Calcium. After deposition, our devices are removed from the evaporator and transfered to the characterization glovebox for testing. Figure 3-11 is an image of the solar cell after deposition of the electrodes. A halogen light is used to improve the visibility of individual layers. The edges of the organic layer were scratched off prior to depositing the electrodes so the calcium/silver layer on the edge region only contacts the glass substrate. Because our organic layers are deposited via spin-coating we have to scratch off the edges of the film with tweezers.

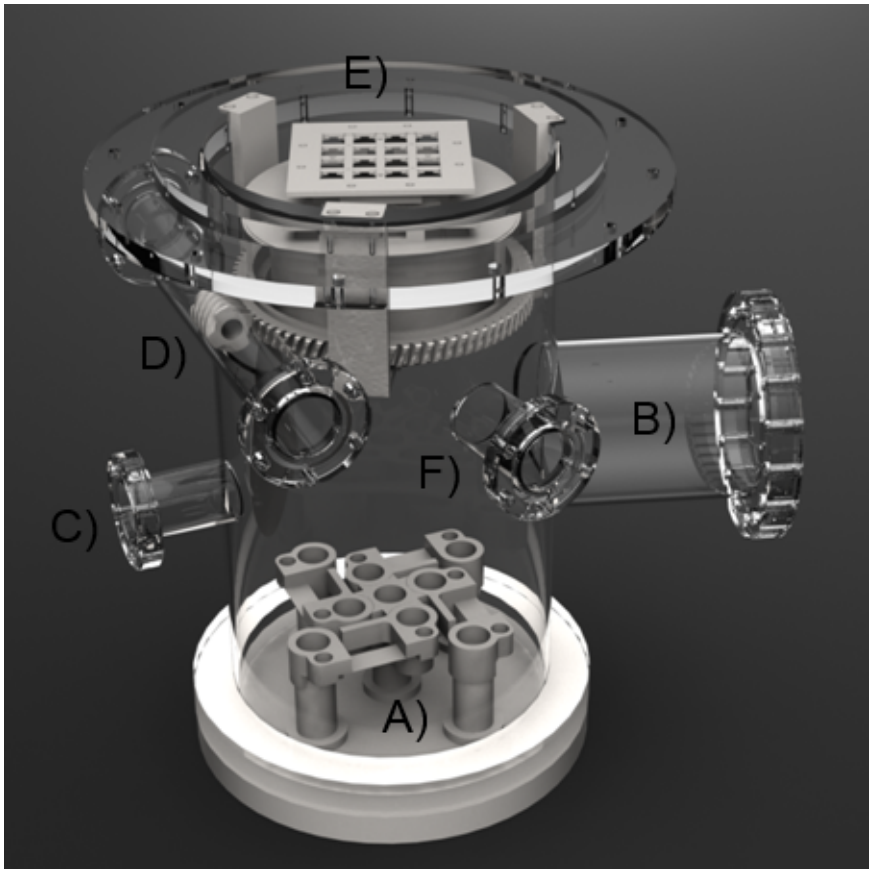

Figure 3-9: Custom Designed Evaporation Chamber with A) Material boats for evaporation B) Turbo pump connection C) Thickness Monitor feed through D) Substrate rotation motor connection E) Substrate placement complete with patterning device F) Viewport

Figure 3-10: Shadow Mask used for deposition of electrodes

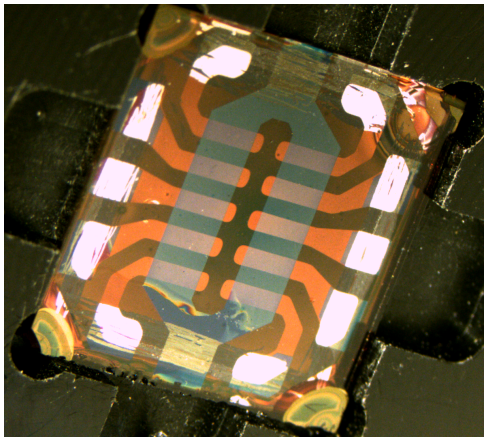

Figure 3-11: Image of organic solar cell after final deposition of electrodes

3.7 Characterization

Our devices are characterized in an inert nitrogen glovebox. Current-Voltage characteristics are taken under dark conditions with a parameter analyzer connected to probes that contact the ITO and silver for each pad on the device. A parameter analyzer is used to generate an I-V curve at a range of applied biases. For light I-V curve measurements an AM1.5 Solar Simulator is used to generate a solar spectrum. Air Mass (AM) is a measure of how much atmosphere sunlight must travel through to reach the earth's surface. A typical value for solar cell measurements is AM 1.5, which means that the sun is at an angle of about 48°. Air mass describes only the spectrum of radiation, not the intensity. For photovoltaics, the intensity commonly used is 100 W/cm^2 [3].

3.8 Fabrication Challenges

Thin films of polymers are notoriously difficult to work with, since they often have poor uniformity, uneven surface morphology, and the molecules with each film are prone to movement within the device after initial deposition.

The morphology of the active layers critically affects the performance of the device. For bi-layer devices, it is somewhat desirable to have a rough interface between the active layers of the device in order to maximize the surface area of the heterojunction, however if the surface roughness of the P3HT film causes irregularities and air pockets in the heterojunction, this can impede charge transfer and thus lower the device's efficiency.

The interface between films has conventionally been improved via thermal annealing [37]. There is a tradeoff, however, because annealing the layers introduces the possibility of mixing between the P3HT and PCBM. Studies of planar device systems show enhancements in cell efficiency after the annealing step [37, 38]. It is unclear however whether this enhancement is due to better contact between the layers or due to intermixing of the layers. The once planar structure may have become a bulk heterojunction and surface area at the heterojunction is now greatly increased. Another reason for enhancements in efficiency is that annealing induces the crystallization of the PCBM, and to a lesser extent, P3HT. Studies have shown that crystallization greatly enhances the ability of PCBM to transport charge. The combination of these potential enhancement effects makes it difficult to identify whether intermixing, better contact at the heterojunction, or increased mobility of the active layer materials is the cause of the efficiency increases.

Our method of stamping allows us to bypass some of these complications by minimizing mixture of the active layers. With this ability, we can attempt to optimize the thickness of each active layer individually in order to gain a better understanding of the physics of charge generation and transport. Several studies have shown that the optimal ratio of these polymers is not a direct ratio of 1:1 P3HT:PCBM. Knowing the optimal thickness of each layer could enable researchers to optimize both planar and bulk heterojunction devices.

Several studies have shown that the thickness of the P3HT active layer should be several times greater than the thickness of the PCBM [27]. The proposed reason for this is the relative carrier transit time of P3HT to PCBM. PCBM has a much longer carrier transit time, and thus it takes longer for an electron to travel through PCBM than it does for a hole to travel through P3HT. Our studies confirm this idea, since the layer of PCBM used in our devices was much thinner than the P3HT.

3.9 Conclusion

The fabrication processes presented in this thesis constitute novel, state-of-the-art, procedures for the Arango Lab at Mount Holyoke College. The fabrication process is notable in several ways. First, the entire fabrication and characterization process takes place within one interconnected glovebox system. After the initial cleaning procedure, devices are never exposed to oxygen or other harmful dust particles. The thermal evaporator used for electrode deposition was designed by students in the Arango lab at Mount Holyoke and offers rapid pump-down times that enable students to fabricate an entire device from start to finish in a short amount of time.

Additionally, the fabrication method used for the fabrication of bi-layer devices is a recently developed method that is new to our laboratory and gives researchers a remarkable amount of control over the active layers in the photovoltaic device. This method has generated a considerable amount of controversy in the literature, and our ability to replicate the procedure gives us an exciting opportunity to report new findings to the scientific community.

Chapter 4

Experimental Results and Comparison to Numerical Simulations

In this work we present the results of a recently developed fabrication method for plastic solar cells. We analyze the morphology of the active layers in the device using atomic force microscopy. We then present the performance of our P3HT:PCBM bulk heterojunction devices and P3HT:PCBM stamped planar heterojunction devices. Our preliminary results for the recently developed method of fabricating planar heterojunction devices demonstrate extremely promising current-voltage characteristics. We then present the results of a simple analytical model for simulating current-voltage in P3HT/PCBM bilayer devices. In an attempt to simulate the more complicated properties of charge transport in organic materials, we utilized a more advanced monte carlo model to calculate the electric field and carrier concentrations in an organic light emitting diode under steady state applied voltage conditions. We propose that the physical processes in this model will be identical to those of organic photovoltaic cells under solar illumination. We analyze the results of

this model and determine them to be physically unrealistic, indicating that further work is necessary in order for these simulations to be compared to our experimental results. We then generate physical insight into the characteristics of our devices by comparing our experimental results to the analytical model.

4.1 Morphology of Active Layers

As mentioned in the previous section, thin films of polymer materials are notoriously difficult to work with, and seemingly standard fabrication processing techniques can result in a host of differing sample results. Our job, then, is to optimize the fabrication processes in our lab in order to develop the most uniformly efficient photovoltaics. We can begin this process by taking optical pictures of our films to record the large scale morphology of our active layer films before deposition of the electrodes. Since the camera in our testing station does not have sufficiently high resolution to look at micron scaled features, we continue the analysis of our film's morphology with the use of an atomic force microscope (AFM). This tool has the ability to determine both the precise thickness (to within several nanometers of error), and the surface roughness of our samples. The samples studied via this method were fabricated specifically for the purpose of studying the morphology under the AFM, pristine P3HT was spin-coated directly to the samples without depositing a layer of PEDOT:PSS first, and PCBM was sequentially stamped for one of the samples. The films were no longer suitable for use as solar cells, since the use of the AFM mandated the removal of the cells from the inert nitrogen environment. Table 4.1 details the samples studied via AFM, with thickness measurements and mean surface roughness as well as maximum variance in height. Figure 4-1 shows images of the surface morphology taken with the

Table 4.1: Film thickness and surface roughness as determined by AFM

Film Description	Thickness	RMS film roughness	Max height	Min height
P3HT spun @ 3000rpm	128.6nm	15.1nm	313nm	168nm
P3HT spun @ 2000rpm	136.9nm	11.1nm	672.7nm	563.7nm
P3HT/2000rpm w/ stamp	160.5nm	15.6nm	569.9nm	447.3nm

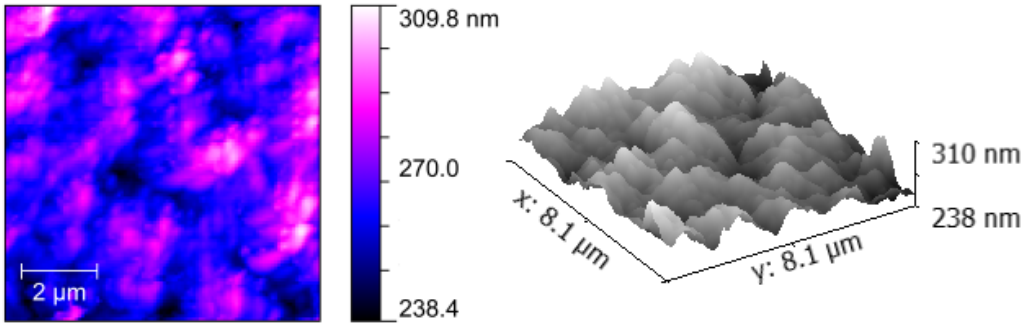

Figure 4-1: AFM Images of the morphology of spin-coated P3HT Films

AFM.

These measurements verify the thickness of each layer and confirm that our stamping procedure does indeed deposit a layer of PCBM on top of the P3HT. Since the films of PCBM are approximately 20 nm thick, the film cannot be seen on the PDMS stamp with a naked eye. The surface roughness data indicates a very rough surface on the P3HT film for the PCBM to adhere to. This will affect the contact between the active layers and could potentially hamper the charge exchange process at the interface.

4.2 Current-Voltage Characteristics of Our Devices

We present the current voltage characteristics of photovoltaic devices fabricated in our laboratory at Mount Holyoke College.

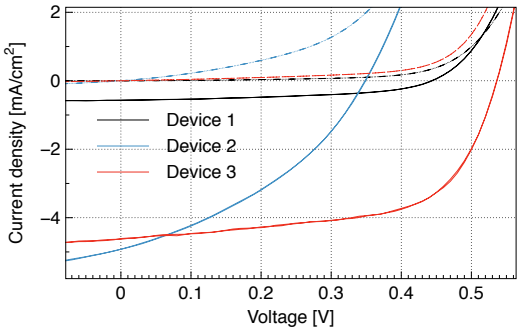

Figure 4-2.a

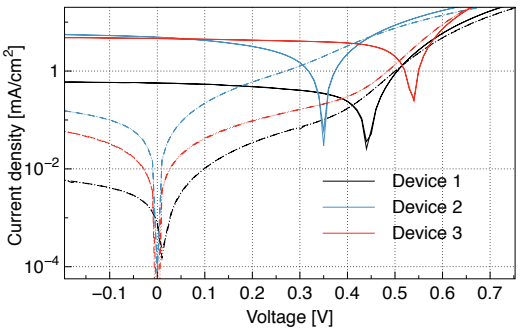

Figure 4-2.b

Figure 4-2: P3HT:PCBM Bulk Heterojunction Device Current-Voltage Characteristics

4.2.1 Bulk Heterojunction Devices

The current-voltage characteristics for two bulk heterojunction devices fabricated in our lab are demonstrated in Figure 4-2. The P3HT:PCBM solution was spun at 800rpm for Device 1, and this yielded J_{SC} = 0.65mA/cm^2, V_{OC} = 0.45 and FF = 0.43. This was our first attempt to fabricate the active layer at this thickness/spin speed. However, many attempts were made to make devices with P3HT:PCBM solution spun at 600rpm. Devices 2 and 3 were made with this spin speed for active layer deposition. The blue curve, Device 2, has one of the highest short circuit currents of our lab's devices to date, yielding J_{SC} = 5mA/cm^2, V_{OC} = 0.35 and FF = 0.34. Device 2 was fabricated by Margaret Stevens. Device 3 has the highest efficiency conversion of a device that has been fabricated in our lab, with J_{SC} = 4.8mA/cm^2, V_{OC} = 0.54V, and FF = 0.585. This device was fabricated by Andrea Miranda. The dramatic increase in efficiency when changing the spin speed of active layer deposition could point to the slower speed optimizing the thickness of the layer, but our results also reflect the number of trials made for films spun at 600rpm. The wide range of efficiency levels in the two devices illustrates how many unknown variables can affect the ultimate efficiency in laboratory

Table 4.2: Current-Voltage Characteristics of P3HT/PCBM Planar Heterojunction Devices

Device	P3HT spin speed	PCBM spin speed	J_{SC} [mA/cm^2]	V_{OC} [V]	FF
1	2000 rpm	1000 rpm	0.0021	0.10	0.29
2	2500 rpm	600 rpm + spin-off	0.0035	0.10	0.35
3	3000 rpm	600 rpm + spin-off	0.0031	0.06	0.27
4	2000 rpm	600 rpm + spin-off	0.00045	0.03	0.37
5	1500 rpm	600 rpm + spin off	-	-	-
6	2000 rpm	none	-	-	-

made devices.

Ultimately, these characteristics still place our devices in a much less efficient category than record holding efficiency levels for P3HT:PCBM bulk heterojunction devices in current literature [12, 13]. Since our lab is a brand new facility we can expect that there will be some inconsistencies in processing that will be improved over the next few years of operation. Taking these bulk heterojunction devices as a reference point, the results of our planar devices are very promising.

4.2.2 Planar Heterojunction Devices

Table 4.2 gives the device specifications for planar devices fabricated and tested in our laboratory. Devices 1-4 produced measurable I-V light and dark characteristics, shown in Figure 4-3. These results indicate a dramatic increase in efficiency level dependent upon the variation of fabrication parameters.The first device we fabricated that turned on, Device 4, had very minimal response under illumination, but subsequent refinement in stamping procedure and film thicknesses improved the efficiency of devices. These results are an amazing outcome for our first attempt at a new device structure in our laboratory. We anticipate similarly dramatic increases in efficiency as the procedure for stamping these devices is refined. These preliminary results are very exciting

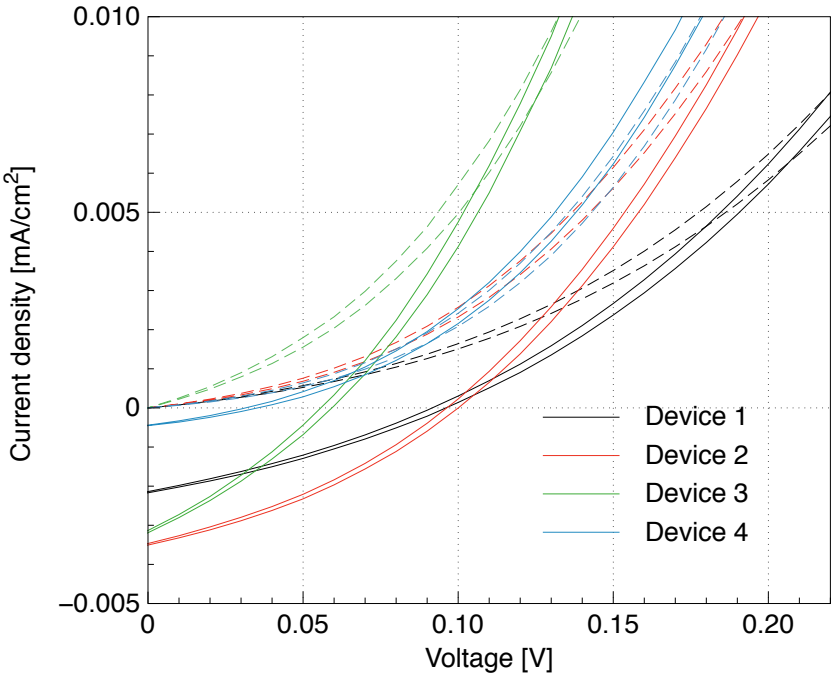

Figure 4-3: IV Characteristics of P3HT/PCBM devices made by stamping the PCBM layer

because they offer insight into the physics of charge transport in these materials and validate the potential of our method for fundamental studies.

Given the roughness of the P3HT film, it is reasonable to assume the the pressure with which the PCBM film is applied plays a large role in the uniformity of the PCBM layer. Studies have shown that the crystal structure of PCBM is strongly linked to the mobility of charge carriers within the material [27] . Ayzner et al. found that the rate limiting material for diffusion of electrons from the heterojunction to the electrodes in P3HT:PCBM bilayer devices was the PCBM layer. For this reason, we kept our PCBM layer much thinner than the P3HT. We also present the current voltage characteristics in log-linear form in Figure 4-4.

All of the devices exhibit extremely high dark current. This indicates that reverse bias injection blocking is bypassed by leakage current from low shunt resistance. The energy band alignment of the two active layers should prevent

any current from flowing in reverse bias, however if either the P3HT or PCBM layer is incomplete, current can "leak" through. This will lead to a decrease in J_{SC} when the device is under illumination. The gradual (rather than sharp) turn-on of the diode indicates that leakage dominates over recombination as the method of current flow in forward bias. This phenomenon leads to a decrease in V_{OC} under illumination. Both the bypass of reverse bias injection blocking and the gradual turn-on of the diode are consistent with an incomplete layer of P3HT or PCBM. From this analysis, however, it is impossible to distinguish which layer causes these effects.

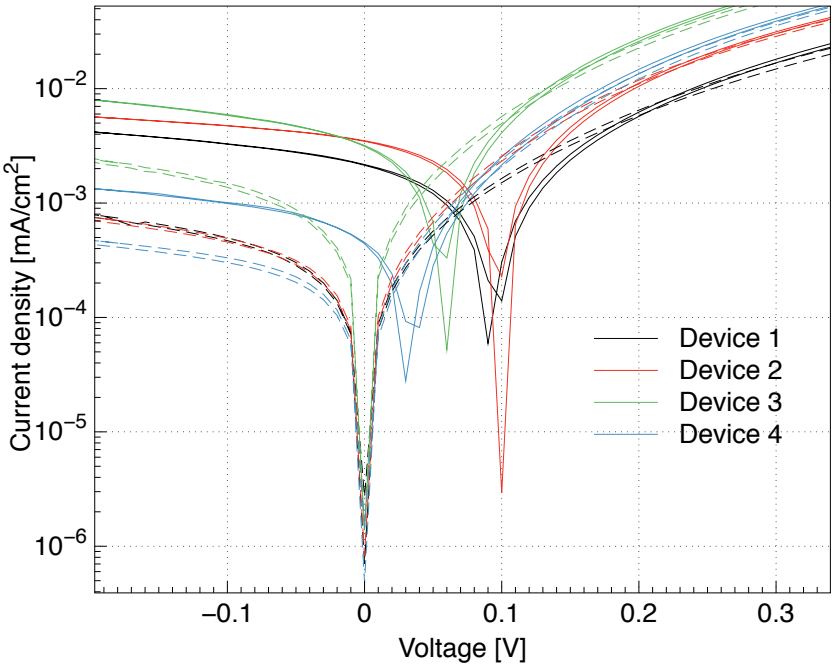

Figure 4-4: Log-linear IV Characteristics of P3HT/PCBM devices made by stamping the PCBM layer

4.3 Modeling the Current-Voltage Characteristics of P3HT/PCBM Planar Devices

We present the results of an analytical model for the current-voltage characteristics of P3HT/PCBM bilayer devices. We then present the results of our analysis of a more sophisticated model for charge transport in organic materials. Our work did not verify the accuracy of this model, and thus our use of this model was limited.

4.3.1 Analytical Model

To compare our results to theoretical current-voltage characteristics for P3HT/PCBM devices we utilize an analytical model written by Ray, et. al. [18]. This model solves for the carrier concentration and electric field in a device and generates an I-V curve under the following algorithm:

- Optical absorption inside the device is calculated by the transfer matrix method [39]. Absorption depends on the complex refractive indices and thicknesses of each layer. The tool assumes AM1.5 solar radiation as an incident spectrum.

- Exciton diffusion for absorbed photons is solved in each layer by Equation 2.6, with the boundary condition that the exciton concentration at the donor-acceptor interface is zero. This is based on the assumption that the exciton dissociation probability is unity at the interface and is field independent.

- The movement of the generated free carriers is approximated by the self consistent solution of the drift-diffusion (Equations 2.10 and 2.11)) and Poisson equations. The generation of these free carriers is calculated from the exciton flux at the the heterojunction and the recombination of free

Table 4.3: Parameters for P3HT/PCBM Bilayer Simulations

Sim #	PCBM μ_h	P3HT μ_e	PCBM LUMO/HOMO	P3HT LUMO/HOMO	P3HT/PCBM Thickness
1	0.0005	0.0001	3/4.9	3.7/6.1	50nm/50nm
2	0.0005	0.0001	3/4.9	3.7/6.1	150nm/20nm
3	0.0001	0.0003	3.1/5	3.7/6.1	150nm/20nm

carriers at the heterojunction is simulated by bi-molecular recombination term.

The model was run under several different operating conditions in order to understand how parameters such as thickness and electron/hole mobility affect the overall I-V characteristics of the system. Details for these simulations are found in Table 4.3.

The interfacial area between the layers of P3HT and PCBM was specified to be 1 nm. This area is where excitons dissociate and also where charge carriers can recombine. The exciton diffusion length for P3HT is 20nm and 5nm for PCBM. These values are consistent with experimental work on exciton diffusion lengths for these materials [40]. The anode material is ITO with a work function of 4.7eV and the cathode is Aluminum with a work function of 3.9eV. The current-voltage characteristics for these simulations are summarized in Figure 4-5.

Both the open circuit voltage and short circuit current decreased when the thickness of the P3HT was increased and the thickness of the PCBM decreased. These parameters were altered to allow for comparison to our experimental devices. The values for LUMO/HOMO used in Device 3 were taken from sigma aldrich. The bandgap of organic materials is known to be highly variable based on orientation and structure of the material. The mobility of majority (and minority) carriers in organic materials is also a highly variable parameter. Approximating these values simplifies our model, with the tradeoff that our results become less physically realistic.

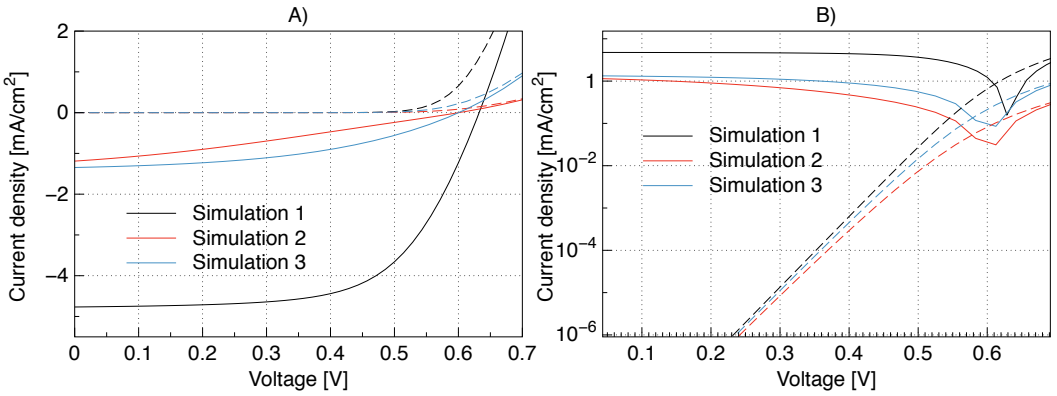

Figure 4-5: Simulated IV Characteristics for P3HT/PCBM Bilayer Devices A) Linear-linear graph and B)Log-linear graph

The results of the simulation show that the thicker P3HT layer in Devices 2 and 3 severely inhibits the generation of photocurrent, resulting in a much lower J_{SC}. Additionally, the Fill Factor of Device 2 is less than that of Device 3, which concurs with the lower P3HT mobility used for Device 2. Physically, this relates to the fact that the amount of photons that reach the lower layers of the P3HT dies off exponentially. With a thick layer of P3HT, there will be less excitons formed near enough to the heterojunction to diffuse across it, generating free carriers. Additionally, Devices 2 and 3 have much lower shunt resistance, correlating to leakage current through the reduced layer of PCBM.

In order to analyze how the devices are functioning in this simulation, we look at where the charge is building up in the device. The model gives us information on the majority carrier concentration throughout the device at steady state. The other relevant parameter is the electric field inside the device. These properties are displayed in Figure 4-6.

The unexpected result of this charge distribution shows that there is a buildup of charge carriers at the electrodes, with no charge build up at the heterojunction. We suspect that the charge build up at the electrodes is due to the diffusion of charge carriers into the organic materials from the higher

(A)

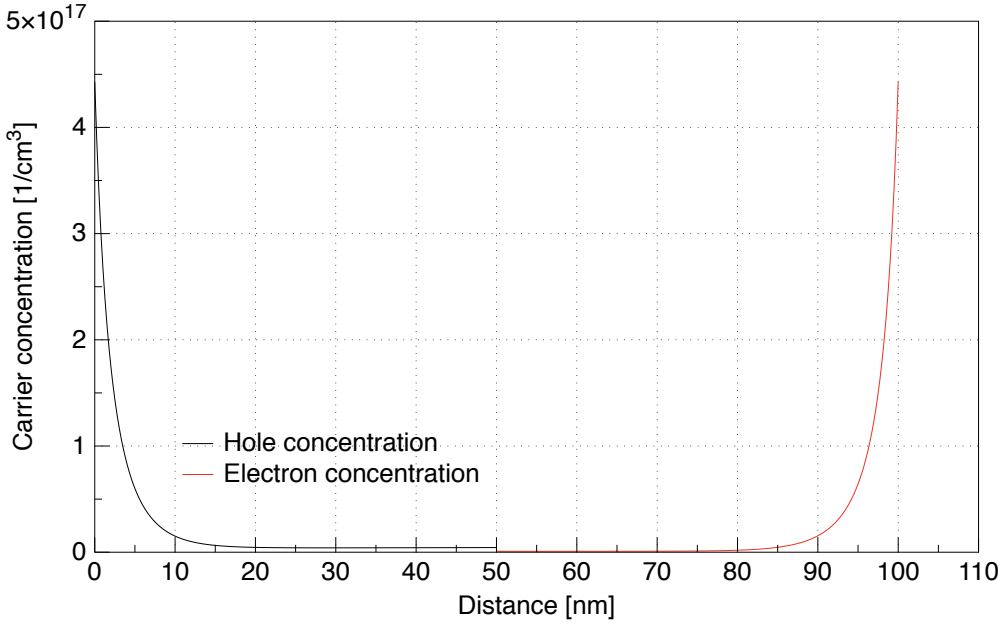

(B)

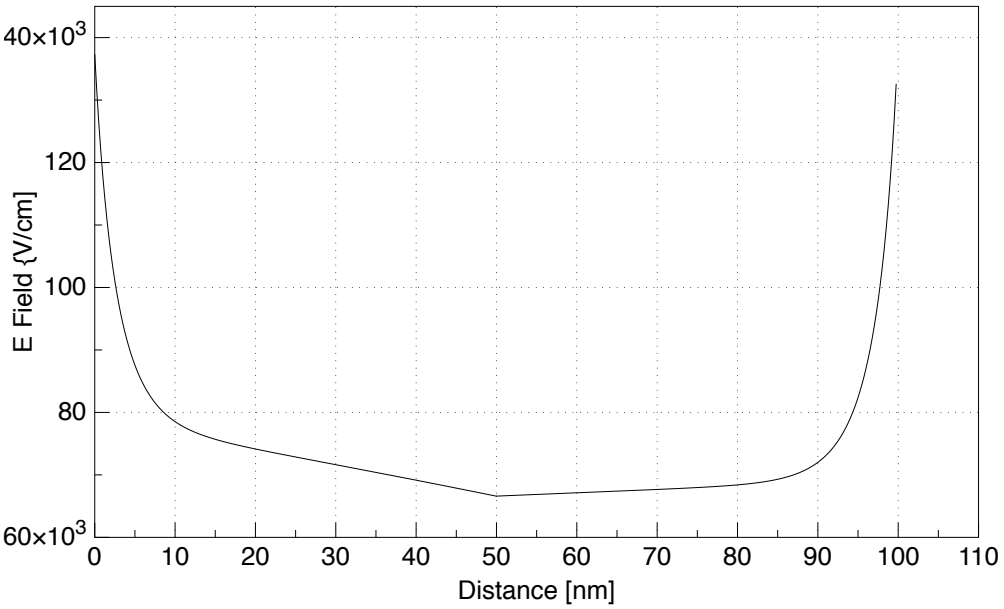

Figure 4-6: Simulated Properties of P3HT/PCBM Bilayer Devices A) Carrier Concentration B) Electric Field

concentration of carriers in the anode/cathode materials. The unexpected result, however, is the lack of charge build up at the heterojunction. This suggests a high amount of carrier recombination at the electrodes (carriers are recombining before they can travel away from the heterojunction). The electric field strength somewhat mirrors the concentration of charge carriers, since the carriers are generating this electric field.

The model does not provide us with the concentration of minority carriers in the device, and so we could not calculate the total current throughout (to make sure that it was constant). Although this model is useful to help us analyze the performance of our devices, it does not help us discover any new physics, because it is limited by the simplifications built in to its calculations. In the next section we present our attempt to reach a molecular scale understanding of our devices with a fundamentally different modeling approach.

4.3.2 Monte Carlo Simulation

The model above presents a very simplified understanding of the physics of solar cells. It relies on the exciton generation equation to determine the generation of excitons, utilizes a simple method of calculating disassociation across the heterojunction, and utilizes the drift diffusion equations to calculate charge transport through the organic materials to the electrodes. As outlined by Chapter 2 of this thesis, use of these approximations requires some vast simplifications. As a result, the simulation can not help us learn new physics, since it is based on what we already know. Our devices are stretching the bounds of current understanding of molecular systems, and thus we need a tool that can generate new insights on the unknown physical processes that are happening.

To attempt this, we utilized a one-dimensional rate model written by Ian Rousseau [41]. The model calculates the movement of polarons in the device.

Polarons are quasi particles that are composed of a charge and the accompanying polarization field. As an electron moves through a solid, it interacts with the lattice ions through long range interactions, carrying distortions in the lattice with it as it moves, also known as a cloud of phonons. Interactions with the lattice phonons are computationally intensive, due to the sheer number of phonons in a solid. This model makes a compromise between the accuracy of a full scale monte carlo model of charge movement and the requirements of processing speed. The movement of polarons is approximated by the Miller-Abrahams model of temperature dependent phonon induced electrical site to site hopping [42].

The model determines where charge and excitons build up in devices in the steady state of operation. It generates a carrier concentration profile, as well as the electric field in the device. The model calculates charge transport and exciton generation leading to photon generation given an externally applied bias. As such, it functions as a light emitting diode instead of a solar cell. The physics inside the device is exactly the same, and the design requirements are similar, except that good absorption depth is not an issue since photons are generated instead of absorbed by excitons.

Rousseau originally ran this model for a Tris(8-hydroxyquinolinato)aluminium - tetraphenylbenzidine (Alq3-TPD) device architecture. The model initially promised agreement with experimental results, generating an I-V curve that replicates the form of physical devices. The simplications of a delta-function density of states, constant hopping rates, and nearest-neighbor exciton transport were used. Polaron and exciton hopping rates were calculated from experimental mobilities. A simple power law was taken for the injected current, in accordance with Limketkai and Baldo's microscopic model [43]. The parameters for this simulation are found in Table 4-7. The preliminary results for this model are shown in Figure 4-8.

A)

Layer	Thickness [cm]	μ_p [cm^2/V-s]	μ_n [cm^2/V-s]	E_L [eV]	E_H [eV]	$\gamma_{np,bulk}$ [cm^3/s]
TPD	4×10^{-6}	1.25×10^{-3}	1.88×10^{-7}	2.1	5.4	1×10^{-14}
Alq_3	4×10^{-6}	1×10^{-7}	1×10^{-5}	3.1	5.8	1×10^{-14}

B)

Layer	Thickness [cm]	E_g [eV]	L_x [cm	τ_x [s]
TPD	4×10^{-6}	2.6	1×10^{-7}	1×10^{-7}
Alq_3	4×10^{-6}	2.4	8×10^{-7}	1×10^{-8}

Figure 4-7: Transport Parameters for simulating a TPD-Alq3 OLED A) Polaron transport parameters. Miller-Abrahams hopping rates are calculated from mobilities (μ) and energy level difference at the heterojunction (E_H and E_L), and $\gamma_{np,bulk}$ is the rate constant for polaron recombination in the bulk B) Exciton transport parameters. Hopping rates calculated from exciton diffusion length,L_x and lifetime τ_x

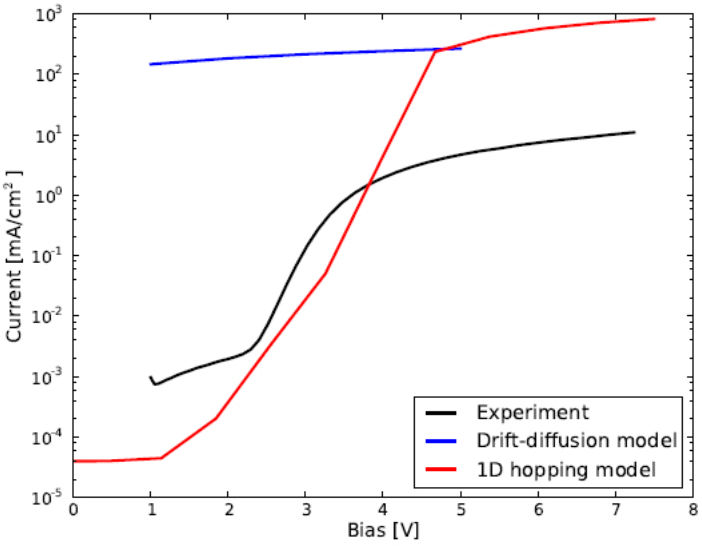

Figure 4-8: Current-Voltage Results for 1-D Monte Carlo Simulations of Alq3-TPD bilayer OLED Device Image credit: Ian Rousseau

The model generates the electric field and carrier concentrations used to calculate current. To check this model against the more general approximation of the drift-diffusion equations we independently calculated the current that would be generated from the direct application of the drift diffusion equations with the model generated electric field and carrier concentrations. We graphed these results in order to understand how the model output coupled with the drift diffusion equations predicts the current throughout the device. Figure 4-9 shows our results.

Our analysis shows that the current is not constant throughout the device. This directly contradicts the physical requirements of current based on Maxwell's equations. At steady state, the current must be constant. To better understand why we were getting this result, we separately calculated the electric field driven current and the diffusion driven current contributions in order to specifically understand how the electric field and carrier concentration gradient individually affected the current. Our results showed that although the diffusion term appeared to be behaving in a physically realistic way, the term driven by the exceptionally large electric field, the drift current, does not behave in a reasonable manner. The high variance in electric field results in an unrealistic drift current that does not reflect the behavior of a physical device.

Some other anomalies that are shown through this analysis are the outlying result at 1V applied bias, and the decrease in current at applied biases between 1V and 3V. These results did not correlate well with the expectation that electric fields within the device increase at higher applied voltages. As a result of the multitude of physical inconsistencies in this model found through our computational analysis, we did not continue the use of this model to simulate P3HT/PCBM devices. The code used to perform our analysis on the output of Rousseau's model was written in MatLab, and is included in Appendix B of this thesis.

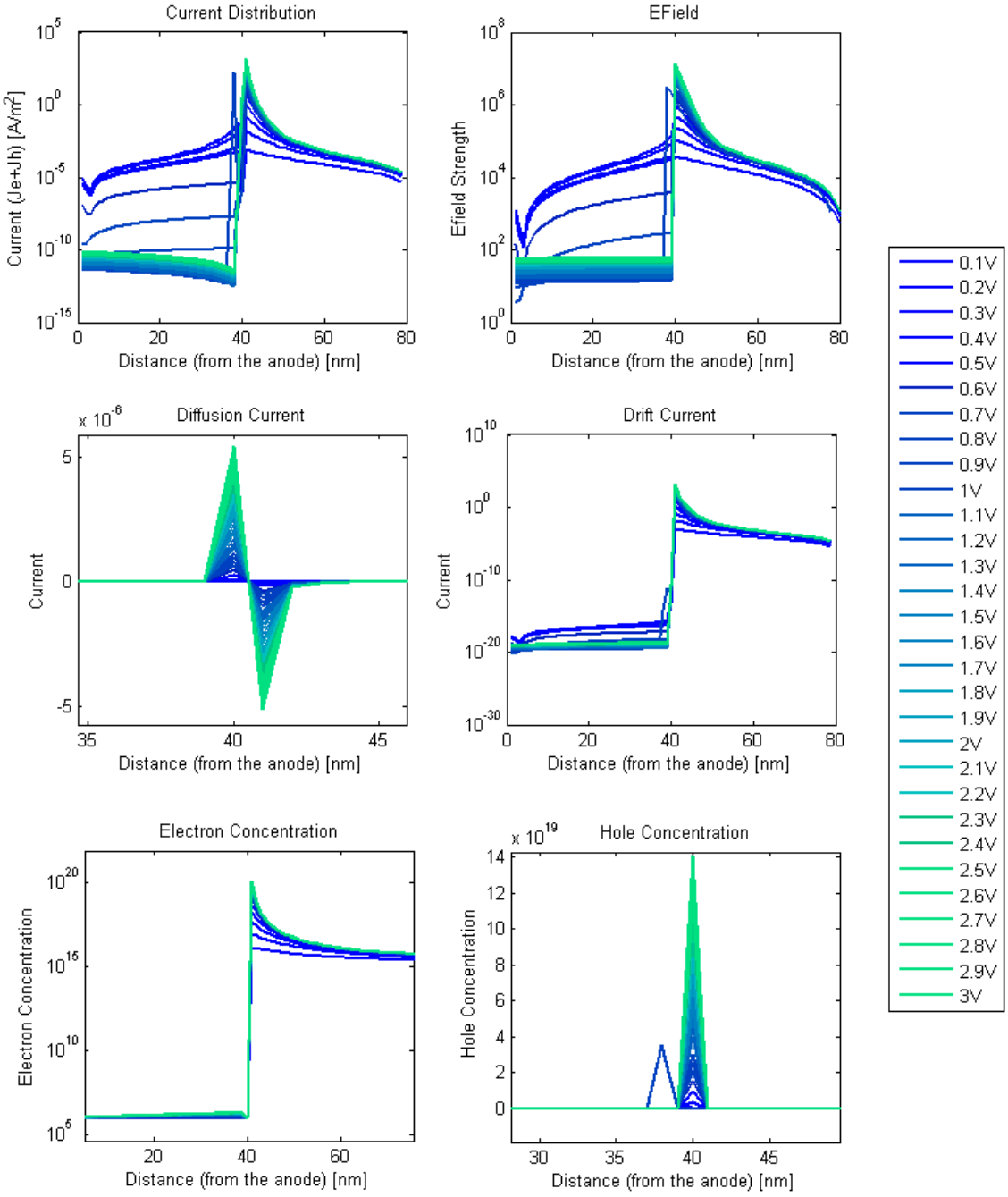

Figure 4-9: Detailed analysis of Rousseau's 1-dimensional monte carlo charge transport model under the approximation of the drift-diffusion equations

4.4 Conclusion

We have presented the results of our bulk heterojunction devices and planar heterojunction devices fabricated in our lab at Mount Holyoke College. Additionally, we have presented our findings from two simulations modeling the current-voltage characteristics of organic photovoltaic devices. The first, an analytical model, confirms our original analysis of the causes for low efficiencies in our planar heterojunction devices. The second, a more advanced model that attempts to incorporate information about interactions with the material's lattice ions and phonons through the simulation of polaron hopping movement, was analyzed in an attempt to find a better description of device characteristics. Our analysis demonstrates that this model fails to yield physically accurate results.

Chapter 5

Conclusions and Future Work

The potential socioeconomic impacts of the invention of efficient organic photovoltaics are enormous. This possibility has motivated us to study the fundamental processes that limit the efficiency of these devices. We have presented the current theoretical understanding of the physics of organic materials in the context of photovoltaics. Much of this physics is not easy to write down, since it involves many uncertainties inherent to the molecular structure of the materials and the amorphous nature of the films. We have presented the usual equations used for approximating the physics in solar cells in order to gain a qualitative understanding of what is happening inside of our devices.

We present the implementation of a recently developed alternative method of fabricating organic photovoltaics. This fabrication process was completed in our lab at Mount Holyoke College. The characteristics of the bi-layer devices fabricated by the method described in this thesis have the advantage of helping us to better understand fundamental charge movement processes in organic photovoltaics.

To analyze our device performance, we utilize an analytical model with the commonly used approximations for charge generation and transport mechanisms. This model confirms our hypothesis about the effect of layer thicknesses

on the current-voltage characteristics of our bi-layer devices.

To further probe the physics of our devices, we used a molecular scaled rate model utilizing monte carlo techniques to simulate charge movement in organic materials under charge injection situations. However, the results of this simulation failed to yield physically realistic results, and so further analysis is necessary before these more advanced calculations can be used to study the results of our devices. The problems found in this model lead us to the further work that we hope to achieve in the Arango lab on this subject.

5.1 Experimental Work

The many remaining questions surrounding charge generation and transport in the active layers of P3HT/PCBM devices suggest further experimental work. One interesting experiment that the author did not have time to complete is the fabrication of a stamped bi-layer device with a reversed order of active layers. By first spin-coating the PCBM and successively stamping the P3HT, the thinner layer of PCBM would now be the only layer that photons need to penetrate before reaching the region near the heterojunction of the device.

This experiment would help us answer two fundamental questions. First, how much loss in efficiency is directly due to the short exciton diffusion length of P3HT. Because the incident photons will no longer have to travel through the layer of P3HT before reaching the region of the film where excitons can generate charge carriers, we may see an increase in efficiency. Second, we can anneal the PCBM before depositing the P3HT. This will allow us to study how crystallinity in the PCBM contributes to the device's efficiency. The comparison of this proposed device structure to the results in this thesis would offer valuable insight on the physical processes at the P3HT/PCBM heterojunction.

5.2 Computational Work

The monte carlo simulations in this thesis were not completed with satisfactory results meriting comparison to our experimental devices. Further work is necessary to understand where the model went wrong, and why it does not internally check for the constancy of the current throughout the simulated device. Perhaps, after further analysis, the model could be adjusted to check for this physical parameter.

5.3 Looking forward

The results presented in this thesis constitute one of the very first experiments in the Arango lab at Mount Holyoke College. The success of this project is an exciting development with implications for the viability of its cutting-edge fabrication method. The project has given us new information about the properties of the organic materials in our devices. The amount of discoveries that are currently taking place in the field of organic photovoltaics makes this area an exciting place for undergraduate students to work. The results of this project demonstrate the potential for further discoveries in this field and illustrate the amazing opportunities that this lab provides for undergraduates to make valuable contributions to solar cell research.

Appendix A

SOP for Fabricating Stamped Bi-layer Devices

This appendix contains the Standard Operating Procedure for the recently developed method of stamp transfer printing. The document has been modeled after the SOP for spin coating P3HT:PCBM Bulk Heterojucntion Devices written by Andrea Miranda and Alexi Arango.

Introduction:

This document describes the procedure for spin coating a film of PEDOT:PSS, a film of P3HT from solution onto an ITO glass substrate, and stamp transferring a film of PCBM onto the P3HT film. The procedures for making the solution of P3HT:PCBM, cleaning ITO glass substrates and evaporating the metal electrodes are described elsewhere. It is good lab practice to keep note of critical information about your device growth, such as spin parameters, time durations, solutions used, unusual observations, equipment difficulties or mistakes. Written notes that are scanned with the scanner will automatically be loaded into evernote.

Before using the wet glovebox, you must sign up for time on the wet glovebox google calendar. You will be given access to the google calendar once you have been certified to use the glovebox by a senior lab member, Len or Alexi. Contact Alexi for access to the google calendar. You can also sign up using the Calendar app on any of the computers or tablets in the lab.

Hazards:

- When working with chemicals in the wet glovebox, put on the appropriate safety gear including goggles, lab coats, and gloves.
- Wear latex gloves on top of glovebox gloves for extra protection
- **Before the use of any chemicals in the glovebox, circulation must be turned off (F5).**
- **If working with a water-based solution such as PEDOT:PSS, auto-purge the glovebox (F6) for the entire time that exposed water is present**
- Before working with substrates,
  -
  - turn on laminar flow to ensure that the atmosphere in the glovebox is free of particles
  - clean the glovebox by blowing pressurized nitrogen towards the back of the glovebox.
  - Clean the gloves by picking up dust particles with the lint roller.

Supplies:

- Clean substrates in fluoroware
- Micropipette and tips
- Plastic-coated tweezers
- Aluminum foil
- Texwipe (to clean spin coater)
- Timer (annealing)

Chemicals:

- PEDOT:PSS solution
- P3HT solution
- PCBM solution
- PDMS Stamps
- Dichlorobenze solution

Procedure:

1. Glovebox Preparation
2.
    1. On a sheet of aluminum foil lay out all supplies to be brought into the glovebox. This may include newly cleaned substrates submerged in isopropanol. For best results, keep as little isopropanol as possible in the beaker. Wrap the aluminum foil around the beaker to prevent any damage in case of a spill
    2. If the solution to be spin-coated is in an opaque jar, you may transfer the approximate amount needed into a colorless vial to see clearly. Label the vial and place in vial tray.
    3. Set the amount of solution needed on the micropipette
3. Set the spin coater
4.
    1. To change a parameter starting at Recipe 1: Press MODE, use the left or right arrow to navigate between the listed parameters (step, ramp, rpm, etc.) and use the up or down arrow to set a desired value, press ENTER, press MODE
    2. Parameter settings:
        - Step: 1
        - Ramp: 0
        - RPM (revolutions per minute): varies from 500 to 1300 rpm
        - Dwell (how long the substrate will spin): 60 s
        - Disp (dispense): none
        - Time: 0 (60 seconds is standard)

1. Spinning
2.
    1. Open the glass cover to the spin coater
    2. Pick up substrate (originally face-down in the fluoroware) and flip it so as to place it face-up onto the o-ring of spin coater
    3. Center and close lid
    4. Stir the polymer solution (a couple of minutes, set speed so that a little depression forms in solution surface)
    5. Attach the pipette tip to the micropipetter
    6. Set the micropipetter volume to 40-50 ul
    7. Withdraw the solution from the vial to the pipette tip
    8. Place a finger from your free hand on the spinner start button
    9. Place the micropipetter directly vertically above the substrate.
    10. Release the solution from the pipetter one drop at a time until the solution uniformly coats the substrate
    11. Press the start button
    12. Dispose of pipette tip
    13. Wait for substrate to stop spinning, open the lid
    14. Pick up the substrate and place it face down in a fluoroware dish
3. Annealing
4.
    1. Turn on hot plate and set to desired temperature (150 C for PEDOT:PSS or 110 C for P3HT)
    2. Wait for the surface to heat up
    3. Set timer for 5 minutes for PEDOT:PSS or 10 minutes for P3HT
    4. Place substrate in the center of the hotplate and start timer
    5. Remove the substrate from the hot plate and place it face down in a fluoroware dish
5. Stamping
    1. Clean PDMS Stamp by placing the stamp on the spin coater, and successively depositing a layer of DCB and spinning the stamp for several seconds.
    2. Make sure to handle the stamp with tweezers on the underside of the stamp
    3. Deposit film of PCBM using spinning procedure outlined above
    4. Remove stamp from spinner and place in case

5. Open the florowave case containing sample with films of PEDOT:PSS and P3HT already deposited
6. Transfer the film of PCBM from the stamp to the sample by firmly pressing the stamp against the sample, one side first, to minimize airpockets. After pressing firmly, pull away the stamp. The film should now be adhered to the surface of the P3HT.

6. Cleaning up
7.
    1. Make sure all vials and containers are closed
    2. Turn off laminar flow once substrates are no longer exposed
    3. Auto-purge (F6) (set for 10 minutes) once or twice depending on how long you've been working with solvents
    4. Remove all waste to the fume hood and dispose of contaminate items in the hazardous waste container
    5. After auto-purge has completed, turn on circulation (F5) and ensure that oxygen and moisture ppm's are at zero

Last edited by:

- Phoebe Tengdin

Appendix B

Simulation Analysis Code

This appendix contains the code written to analyze the output of Rousseau's computational model using the drift diffusion approximation for charge transport. This code was written to run in MatLab. To run the code, the user must have access to ouput files from Rousseau's model. These files must be stored in a folder hierarchy organized by the applied voltage given when running each iteration of Rousseau's model. This can be seen by the file name structure specified by the attached code.

```
clear all;
clear;
CHECK = 0;
MINVOLT = 1;
MAXVOLT = 5; %voltage range %%not doing it this way anymore
%EMOBP = 1*10^(-8); %electron mobility of p-type material
[m^2/V*s]
EMOBN = 1*10^(-4); %electron mobility of n-type material
HMOBP = 5*10^(-4); %hole mobility of p-type material [m^2/V*s]
%HMOBN = 1*10^(-8); %hole mobility of n-type material
T = 300; %[K]
K = 1.3806503 * 10^-23; % Boltsman [m^2 kg s^-2 K^-1]
Q = 1.60217646 * 10^-19; %charge of an electron
%EDIFFUSIONP = K*T*EMOBP./Q; %electron Diffuson coefficient p
type material
EDIFFUSIONN = K*T*EMOBN./Q; %electron Diffuson coefficient n type
material
HDIFFUSIONP = K*T*HMOBP./Q; %hole Diffuson coefficient p type
material
%HDIFFUSIONN = K*T*HMOBN./Q; %hole Diffuson coefficient n type
material
DEVAREA = 1; %device area
DeviceName = 'OPVTool Simulation\';
InVval = 30; %number of increments in the voltage inputs
cmap = winter(InVval);


i=1;
%read in the values from the model
Efield = dlmread( strcat(DeviceName, 'Electricfield.txt'),',');
EConc = dlmread( strcat(DeviceName,
'ElectronConcentration.txt'),',');
HConc = dlmread( strcat(DeviceName, 'HoleConcentration.txt'),',');
%ElecPot = dlmread( strcat(DeviceName, volt,
'V\Electrostaticpotential.txt'),',',6,0);

%calculates electron contribution to the current in the ptype
material
% for k = 1:(length(Efield))/2 -1;
%     J_drift_e(k,i) = Q*(EConc(k,2)*EMOBP*Efield(k,2));
%     J_diff_e(k,i) = Q*(EDIFFUSIONP*((EConc(k+1,2)-
EConc(k,2))/(EConc(k+1,1)-EConc(k,1))));
%     Je(k,i) = J_drift_e(k,i) + J_diff_e(k,i);
% end

%calculates electron contribution to the current in the ntype
material
for k =(length(Efield)-1)/2:(length(Efield)-2)
    l=k-198;
    J_drift_e(l,i) = Q*(EConc(l,2)*EMOBN*Efield(k,2));
    J_diff_e(l,i) = Q*(EDIFFUSIONN*((EConc(l+1,2)-
EConc(l,2))/(EConc(l+1,1)-EConc(l,1))));
    Je(k,i) = J_drift_e(l,i) + J_diff_e(l,i);
end
```

```
%calculates hole contribution to the current in the ptype
material
for p = 1:(length(Efield)-2);
    if p>198
        J_drift_h(p,i) = 0;
        J_diff_h(p,i) = 0;
    else
    J_drift_h(p,i) = Q*(HConc(p,2)*HMOBP*Efield(p,2));
    J_diff_h(p,i) = Q*( HDIFFUSIONP*((HConc(p+1,2)-
HConc(p,2))/(HConc(p+1,1)-HConc(p,1))));
    end
    Jh(p,i) = J_drift_h(p,i) + J_diff_h(p,i);
end

% %calculates hole contribution to the current in the ntype
material
% for n = (length(Efield))/2:(length(Efield)-1);
%     J_drift_h(n,i) = Q*(HConc(n,2)*HMOBN*Efield(n,2));
%     J_diff_h(n,i) = Q*(HDIFFUSIONN*((HConc(n+1,2)-
HConc(n,2))/(HConc(n+1,1)-HConc(n,1))));
%     Jh(n,i) = J_drift_h(n,i) + J_diff_h(n,i);
% end

hold all

%total current is Je + Jh
Jcomp = bsxfun(@plus, Je, Jh);
%Jcomp(1:length(Efield)-1,i) =
(Je((length(Efield)/2):(length(Efield)-
1),i))+(Jh(1:(length(Efield)/2-1),i));

%plot the different plots

subplot(2,3,1)
semilogy(Jcomp(:,i),...
    'LineWidth',2);
%hleg1 = legend('show');
%set(hleg1,'Location','NorthWest')
title(' Current Distribution ')
xlabel('Distance (from the anode) [nm]')
ylabel('Current (Je+Jh) [A/m^2]')

subplot(2,3,2)
semilogy(Efield(:,2),'LineWidth',2);
title(' EField ')
xlabel('Distance (from the anode) [nm]')
ylabel('Efield Strength')

subplot(2,3,3)
semilogy(J_drift_e(:,i),'LineWidth',2)
title(' Drift Current ')
xlabel('Distance (from the anode) [nm]')
ylabel('Current')

subplot(2,3,4)
```

```
plot(J_diff_e(:,i),'LineWidth',2)
title('Diffusion Current')
xlabel('Distance (from the anode) [nm]')
ylabel('Current')

subplot(2,3,5)
plot(HConc(:,2),'LineWidth',2)
title('Hole Concentration')
xlabel('Distance (from the anode) [nm]')
ylabel('Hole Concentration')

subplot(2,3,6)
semilogy(EConc(:,2),'LineWidth',2)
title(' Electron Concentration ')
xlabel('Distance (from the anode) [nm]')
ylabel('Electron Concentration')
```

Bibliography

[1] Department of Energy (DOE) Energy Information Administration (EIA), 2013.

[2] Jenny Nelson. *The Physics of Solar Cells*. Imperial College Press, London, UK, 2003.

[3] TL Benanti and D. Venkataraman. Organic solar cells: An overview focusing on active layer morphology. *Photosynthesis Research*, 87(1):73–81, JAN 2006. PT: J; NR: 26; TC: 67; J9: PHOTOSYNTH RES; PG: 9; GA: 042CO; UT: WOS:000237505100008.

[4] Holger Spanggaard and Frederik C. Krebs. A brief history of the development of organic and polymeric photovoltaics. *Solar Energy Materials and Solar Cells*, 83(23):125 – 146, 2004. ¡ce:title¿The development of organic and polymer photovoltaics¡/ce:title¿.

[5] Jesus delAlamo. *Microelectronic Devices: Physics and Modeling*. Prentice Hall, 2009.

[6] T. L. Benanti and D. Venkataraman. Organic solar cells: An overview focusing on active layer morphology. *Photosynthesis Research*, 87(1):73–81, JAN 2006 2006. PT: J; TC: 67; UT: WOS:000237505100008.

[7] Dian Chen, Atsuhiro Nakahara, Dongguang Wei, Dennis Nordlund, and Thomas P. Russell. P3ht/pcbm bulk heterojunction organic photo-

voltaics: Correlating efficiency and morphology. *Nano Letters*, 11(2):561–567, FEB 2011. PT: J; NR: 48; TC: 84; J9: NANO LETT; PG: 7; GA: 717LZ; UT: WOS:000287049100043.

[8] Y. Kim, SA Choulis, J. Nelson, DDC Bradley, S. Cook, and JR Durrant. Device annealing effect in organic solar cells with blends of regioregular poly(3-hexylthiophene) and soluble fullerene. *Applied Physics Letters*, 86(6):063502, FEB 7 2005. PT: J; NR: 18; TC: 334; J9: APPL PHYS LETT; PG: 3; GA: 902KQ; UT: WOS:000227355200073.

[9] Sung H. Park, Anshuman Roy, Serge Beaupre, Shinuk Cho, Nelson Coates, Ji S. Moon, Daniel Moses, Mario Leclerc, Kwanghee Lee, and Alan J. Heeger. Bulk heterojunction solar cells with internal quantum efficiency approaching 100 *Nature Photonics*, 3(5):297–U5, MAY 2009. PT: J; NR: 41; TC: 1433; J9: NAT PHOTONICS; PG: 7; GA: 447UY; UT: WOS:000266218600014.

[10] SE Shaheen, CJ Brabec, NS Sariciftci, F. Padinger, T. Fromherz, and JC Hummelen. 2.5 *Applied Physics Letters*, 78(6):841–843, FEB 5 2001. PT: J; NR: 16; TC: 1607; J9: APPL PHYS LETT; PG: 3; GA: 398CF; UT: WOS:000166737800053.

[11] Valentin D. Mihailetchi, Hangxing Xie, Bert de Boer, Lacramioara M. Popescu, Jan C. Hummelen, Paul W. M. Blom, and L. J. A. Koster. Origin of the enhanced performance in poly(3-hexylthiophene): [6,6]-phenyl c-61-butyric acid methyl ester solar cells upon slow drying of the active layer. *Applied Physics Letters*, 89(1):012107, JUL 3 2006. PT: J; NR: 20; TC: 112; J9: APPL PHYS LETT; PG: 3; GA: 061CQ; UT: WOS:000238849200035.

[12] G. Li, V. Shrotriya, Y. Yao, and Y. Yang. Investigation of annealing effects and film thickness dependence of polymer solar cells based on poly(3-hexylthiophene). *Journal of Applied Physics*, 98(4):043704, AUG 15 2005. PT: J; NR: 19; TC: 351; J9: J APPL PHYS; PG: 5; GA: 959XD; UT: WOS:000231551700056.

[13] Svetlana S. van Bavel, Maik Baerenklau, Gijsbertus de With, Harald Hoppe, and Joachim Loos. P3ht/pcbm bulk heterojunction solar cells: Impact of blend composition and 3d morphology on device performance. *Advanced Functional Materials*, 20(9):1458–1463, MAY 10 2010. PT: J; NR: 38; TC: 70; J9: ADV FUNCT MATER; PG: 6; GA: 598BD; UT: WOS:000277806000012.

[14] A. C. Mayer, Michael F. Toney, Shawn R. Scully, Jonathan Rivnay, Christoph J. Brabec, Marcus Scharber, Marcus Koppe, Martin Heeney, Iain McCulloch, and Michael D. McGehee. Bimolecular crystals of fullerenes in conjugated polymers and the implications of molecular mixing for solar cells. *Advanced Functional Materials*, 19(8):1173–1179, APR 23 2009. PT: J; NR: 27; TC: 140; J9: ADV FUNCT MATER; PG: 7; GA: 442QM; UT: WOS:000265855700004.

[15] Almantas Pivrikas, Philipp Stadler, Helmut Neugebauer, and Niyazi S. Sariciftci. Substituting the postproduction treatment for bulk-heterojunction solar cells using chemical additives. *Organic Electronics*, 9(5):775–782, OCT 2008. PT: J; NR: 39; TC: 47; J9: ORG ELECTRON; PG: 8; GA: 347IJ; UT: WOS:000259133500031.

[16] WL Ma, CY Yang, X. Gong, K. Lee, and AJ Heeger. Thermally stable, efficient polymer solar cells with nanoscale control of the interpenetrating network morphology. *Advanced Functional Materials*, 15(10):1617–1622,

OCT 2005. PT: J; NR: 30; TC: 2307; J9: ADV FUNCT MATER; PG: 6; GA: 976VL; UT: WOS:000232761500008.

[17] Yun Zhao, Zhiyuan Xie, Yao Qu, Yanhou Geng, and Lixiang Wang. Solvent-vapor treatment induced performance enhancement of poly(3-hexylthiophene): methanofullerene bulk-heterojunction photovoltaic cells. *Applied Physics Letters*, 90(4):043504, JAN 22 2007. PT: J; NR: 13; TC: 139; J9: APPL PHYS LETT; PG: 3; GA: 130HC; UT: WOS:000243789600104.

[18] Biswajit Ray, Camila Andrea Gonzlez Williamson, Mohammad Ryyan Khan, and Muhammad A. Alam. Opv lab, Oct 2011.

[19] W. J. Potscavage, S. Yoo, and B. Kippelen. Origin of the open-circuit voltage in multilayer heterojunction organic solar cells. *Applied Physics Letters*, 93(19):193308, NOV 10 2008. PT: J; NR: 21; TC: 59; J9: APPL PHYS LETT; PG: 3; GA: 373AT; UT: WOS:000260944100112.

[20] Thomas C. Hayes and Paul Horowitz. *Student manual for the art of electronics*. Cambridge University Press, 1989.

[21] Alexi C. Arango. High open-circuit voltage in heterojunction photovoltaics containing a printed colloidal quantum-dot photosensitive layer, 2010.

[22] J. Nelson, J. Kirkpatrick, and P. Ravirajan. Factors limiting the efficiency of molecular photovoltaic devices. *Physical Review B*, 69(3):035337, JAN 2004. PT: J; NR: 44; TC: 93; J9: PHYS REV B; PG: 11; GA: 773EB; UT: WOS:000188883800081.

[23] Koen Vandewal, Kristofer Tvingstedt, Abay Gadisa, Olle Inganas, and Jean V. Manca. On the origin of the open-circuit voltage of polymer-fullerene solar cells. *Nature Materials*, 8(11):904–909, NOV 2009. PT:

J; NR: 42; TC: 196; J9: NAT MATER; PG: 6; GA: 509WR; UT: WOS:000271050500021.

[24] Keng-Hoong Yim, Zijian Zheng, Ziqi Liang, Richard H. Friend, Wilhelm T. S. Huck, and Ji-Seon Kim. Efficient conjugated-polymer optoelectronic devices fabricated by thin-film transfer-printing technique. *Advanced Functional Materials*, 18(7):1012–1019, APR 11 2008. PT: J; NR: 47; TC: 46; J9: ADV FUNCT MATER; PG: 8; GA: 293RD; UT: WOS:000255351500004.

[25] Toby A. Ferenczi, Jenny Nelson, Colin Belton, Amy M. Ballantyne, Mariano Campoy-Quiles, Felix M. Braun, and Donal D. Bradley. Planar heterojunction organic photovoltaic diodes via a novel stamp transfer process. *Journal of Physics: Condensed Matter*, 20(47):475203, 2008.

[26] Dong H. Wang, Dae-Geun Choi, Ki-Joong Lee, Sang H. Im, O. O. Park, and Jong H. Park. Unexpected solid-solid intermixing in a bilayer of poly(3-hexylthiophene) and [6,6]-phenyl c61-butyric acidmethyl ester via stamping transfer. *Organic Electronics*, 11(8):1376–1380, AUG 2010. PT: J; NR: 28; TC: 18; J9: ORG ELECTRON; PG: 5; GA: 629JV; UT: WOS:000280194400007.

[27] Alexander L. Ayzner, Christopher J. Tassone, Sarah H. Tolbert, and Benjamin J. Schwartz. Reappraising the need for bulk heterojunctions in polymer-fullerene photovoltaics: The role of carrier transport in all-solution-processed p3ht/pcbm bilayer solar cells. *Journal of Physical Chemistry C*, 113(46):20050–20060, NOV 19 2009. PT: J; NR: 53; TC: 80; J9: J PHYS CHEM C; PG: 11; GA: 516ZX; UT: WOS:000271583600039.

[28] Mos Casalegno, Chiara Carbonera, Silvia Luzzati, and Guido Raos. Coarse-grained kinetic modelling of bilayer heterojunction organic solar cells. *Organic Electronics*, 13(5):750–761, 5 2012.

[29] C. Madigan and V. Bulovic. Modeling of exciton diffusion in amorphous organic thin films. *Physical Review Letters*, 96(4):046404, FEB 3 2006. PT: J; NR: 23; TC: 28; J9: PHYS REV LETT; PG: 4; GA: 009AN; UT: WOS:000235083600066.

[30] Conor Madigan and Vladimir Bulovic. Exciton energy disorder in polar amorphous organic thin films: Monte carlo calculations. *Physical Review B*, 75(8):081403, FEB 2007. PT: J; NR: 17; TC: 5; J9: PHYS REV B; PG: 4; GA: 140VC; UT: WOS:000244533800010.

[31] PK Watkins, AB Walker, and GLB Verschoor. Dynamical monte carlo modelling of organic solar cells: The dependence of internal quantum efficiency on morphology. *Nano Letters*, 5(9):1814–1818, SEP 2005. PT: J; NR: 28; TC: 117; J9: NANO LETT; PG: 5; GA: 965JB; UT: WOS:000231945500033.

[32] CM Ramsdale, JA Barker, AC Arias, JD MacKenzie, RH Friend, and NC Greenham. The origin of the open-circuit voltage in polyfluorene-based photovoltaic devices. *Journal of Applied Physics*, 92(8):4266–4270, OCT 15 2002. PT: J; NR: 17; TC: 145; J9: J APPL PHYS; PG: 5; GA: 599DC; UT: WOS:000178318000014.

[33] VD Mihailetchi, LJA Koster, and PWM Blom. Effect of metal electrodes on the performance of polymer : fullerene bulk heterojunction solar cells. *Applied Physics Letters*, 85(6):970–972, AUG 9 2004. PT: J; NR: 11; TC: 70; J9: APPL PHYS LETT; PG: 3; GA: 843TM; UT: WOS:000223109500040.

[34] CH HENRY. Limiting efficiencies of ideal single and multiple energy-gap terrestrial solar-cells. *Journal of Applied Physics*, 51(8):4494–4500, 1980. PT: J; NR: 23; TC: 309; J9: J APPL PHYS; PG: 7; GA: KE107; UT: WOS:A1980KE10700081.

[35] W. SHOCKLEY and HJ QUEISSER. Detailed balance limit of efficiency of p-n junction solar cells. *Journal of Applied Physics*, 32(3):510–512, 1961. PT: J; NR: 46; TC: 1348; J9: J APPL PHYS; PG: 0; GA: 3759B; UT: WOS:A19613759B00146.

[36] A. M. Nardes, M. Kemerink, M. M. de Kok, E. Vinken, K. Maturova, and R. A. J. Janssen. Conductivity, work function, and environmental stability of pedot:pss thin films treated with sorbitol. *Organic Electronics*, 9(5):727–734, 10 2008.

[37] U. Zhokhavets, T. Erb, H. Hoppe, G. Gobsch, and NS Sariciftci. Effect of annealing of poly(3-hexylthiophene)/fullerene bulk heterojunction composites on structural and optical properties. *Thin Solid Films*, 496(2):679–682, FEB 21 2006. PT: J; NR: 19; TC: 79; J9: THIN SOLID FILMS; PG: 4; GA: 995SR; UT: WOS:000234124700081.

[38] XN Yang, J. Loos, SC Veenstra, WJH Verhees, MM Wienk, JM Kroon, MAJ Michels, and RAJ Janssen. Nanoscale morphology of high-performance polymer solar cells. *Nano Letters*, 5(4):579–583, APR 2005. PT: J; NR: 35; TC: 725; J9: NANO LETT; PG: 5; GA: 917NI; UT: WOS:000228468800004.

[39] LAA Pettersson, LS Roman, and O. Inganas. Modeling photocurrent action spectra of photovoltaic devices based on organic thin films. *Journal of Applied Physics*, 86(1):487–496, JUL 1 1999. PT: J; NR: 30; TC: 440; J9: J APPL PHYS; PG: 10; GA: 206BN; UT: WOS:000080856300062.

[40] Jorge Piris, Tieneke E. Dykstra, Artem A. Bakulin, Paul H. M. van Loosdrecht, Walter Knulst, M. T. Trinh, Juleon M. Schins, and Laurens D. A. Siebbeles. Photogeneration and ultrafast dynamics of excitons and charges in p3ht/pcbm blends. *Journal of Physical Chemistry C*, 113(32):14500–14506, AUG 13 2009. PT: J; NR: 41; TC: 91; J9: J PHYS CHEM C; PG: 7; GA: 479LQ; UT: WOS:000268661300066.

[41] Ian Rousseau. Physics and simulation of transport processes in hybrid organic semiconductor devices, June 2010.

[42] A. MILLER and E. ABRAHAMS. Impurity conduction at low concentrations. *Physical Review*, 120(3):745–755, 1960. PT: J; NR: 28; TC: 1605; J9: PHYS REV; PG: 11; GA: WC106; UT: WOS:A1960WC10600014.

[43] Benjie Limketkai. Charge- carrier transport in amorphous organic semiconductors, 2008.